
ORACLE: Explaining Feature Interactions in Neural Networks with ANOVA

Dongseok Kim^{*1} Hyongsun Choi^{*1} Mohamed Jismy Aashik Rasool^{*1} Gisung Oh¹

Abstract

We introduce ORACLE, a framework that explains neural networks on tabular and scientific design data. It fits ANOVA-style main and pairwise interaction effects to a model’s prediction surface. ORACLE treats a trained network as a black-box response, learns an orthogonal factorial surrogate on a discretized input grid, and uses simple centering and μ -rebalancing steps to obtain main- and interaction-effect tables that remain L^2 -consistent with the original model. The resulting grid-based interaction maps are easy to visualize, comparable across backbones, and directly connected to classical design-of-experiments analyses. On synthetic factorial and low- to medium-dimensional tabular regression benchmarks, ORACLE more accurately recovers ground-truth ANOVA interactions and hotspot structure than Monte Carlo SHAP-family interaction methods, as measured by ranking, localization, and cross-backbone stability metrics. In latent image and text settings, ORACLE instead delineates its natural scope, and our results indicate that grid-based ANOVA surrogates are most effective when features admit interpretable factorial structure, making ORACLE particularly well-suited to scientific and engineering tabular workflows that require stable, DoE-style interaction summaries.

1. Introduction

Modern neural networks often rely on rich *interactions* between features rather than purely additive structure, which makes them both powerful and difficult to interpret. Beyond marginal feature importance, practitioners increasingly need tools that describe how features act jointly, how such effects vary across the input space, and whether these patterns remain stable when the backbone model is changed. This need is particularly acute in scientific and engineering tabular set-

tings, where inputs represent physical or design variables and stakeholders value stable, low-order interaction summaries that connect back to classical DoE practice. In this regime, analysis-of-variance (ANOVA) provides a natural formalism: it decomposes a response into main and interaction effects and, in classical design-of-experiments (DoE), uses factorial designs to estimate and visualize interactions with orthogonality and simple diagnostics.

In the neural network setting, most interaction explanations have grown out of the SHAP literature rather than DoE, relying on Monte Carlo sampling over feature subsets and often lacking a clear reference notion of an interaction surface. SHAP interaction indices and related methods can be computationally expensive, sensitive to sampling choices, and difficult to validate in terms of interaction detection, hotspot localization, and transfer across backbones. We instead revisit the DoE perspective and treat a trained neural network as a black-box response surface on which a factorial ANOVA surrogate is fitted. Our framework, **ORACLE** (Orthogonal and Residual ANOVA for Concordant L^2 -Effect Explanations), learns an orthogonal surrogate on a discretized input grid and applies residual centering and μ -rebalancing to recover main-effect and pairwise-interaction tables that remain faithful to the model in an L^2 sense. The resulting low-dimensional ANOVA interaction maps are directly visualizable, comparable across backbones, and aligned with DoE-style reasoning for tabular and scientific-design applications where features admit interpretable factorial structure and stakeholders value stable, low-order interaction summaries.

Contributions.

1. Formulate an ANOVA-based surrogate for neural predictors that yields orthogonal main and pairwise interaction tables with explicit L^2 semantics and associated interaction maps.
2. Define target ANOVA interaction strengths and maps from non-additive residuals on two-dimensional grids, providing a model-centric reference surface for evaluating interaction explanations.
3. Introduce a compact evaluation protocol and metric set that jointly assess interaction selection, hotspot

^{*}Equal contribution ¹Department of Computer Engineering, Gachon University, Seongnam, Gyeonggi, Republic of Korea. Correspondence to: Gisung Oh <eustia@gachon.ac.kr>.

localization, cross-backbone transfer, scale alignment, and intervention-oriented utility.

- Empirically compare ORACLE to SHAP-family interaction methods on synthetic factorial and real tabular regression benchmarks, highlighting regimes in which ANOVA surrogates yield more accurate and stable interaction explanations for low- to medium-dimensional tabular and scientific-design data.

2. Related Work

Global feature interaction explanations. Recent work on global interaction explanations has largely built on the Shapley framework. Faith-Shap introduces an axiomatic Shapley interaction index as a canonical notion of global interaction strength (Tsai et al., 2023), while SHAP-IQ, SVARM-IQ, and KernelSHAP-IQ provide Monte Carlo and kernel-based schemes to efficiently approximate any-order Shapley interactions in practice (Fumagalli et al., 2023; Kolpaczki et al., 2024; Fumagalli et al., 2024). These algorithms and variants are consolidated and benchmarked in the `shapiq` library, which compares Shapley-based interaction estimators across models and datasets (Muschalik et al., 2024). Complementary work analyzes how global feature effects decompose into main and interaction components (Herbinger et al., 2024) and uses Shapley interactions to probe structured phenomena such as syntax and speech representations in large models (Singhvi et al., 2024). However, these approaches mostly return scalar interaction indices rather than explicit ANOVA interaction maps, and are rarely evaluated against an interaction oracle or for stability across backbones.

ANOVA and design-of-experiments views on interactions. Functional ANOVA has re-emerged as a central tool for interpretable machine learning, motivating intrinsically interpretable models that decompose predictions into main effects and low-order interactions, as well as neural architectures that directly parameterize ANOVA components or screen interactions before fitting an ANOVA-style surrogate, enabling higher-order terms with statistical guarantees (Hu et al., 2025; Köhler et al., 2025; Choi et al., 2025; Park et al., 2025). In engineering design and global sensitivity analysis, interpretable neural networks are combined with functional ANOVA decompositions and grouped sensitivity indices to study complex physical interactions from observational data (Dolar et al., 2024). Complementary work in design-of-experiments couples factorial and fractional-factorial designs with modern machine learning to estimate main and interaction effects efficiently in industrial settings (Fontana et al., 2023; Zubair et al., 2024). Our work adopts this ANOVA/DoE perspective but targets pairwise ANOVA interaction maps of a fixed neural backbone and

benchmarks interaction explanation methods, rather than proposing another globally additive predictive model.

Visualization of pairwise effects in regression models. A complementary line of work develops 2D visualizations of how feature pairs jointly affect predictions. Regional effect plots and their extensions, including DALE and recent fast pipelines, efficiently generate ALE/PDP-style 2D regional plots across many features and models (Herbinger et al., 2022; Gkolemis et al., 2023; 2024a). The *vivid* framework and PDPilot further support heatmaps and interactive analytics for ranking and exploring 1D/2D effect patterns (Ingilis et al., 2022; Kerrigan et al., 2025), while toolkits such as Effector integrate these regional explanations into Python workflows (Gkolemis et al., 2024b). Beyond these plotting systems, transformed-feature-space approaches summarize joint and interaction effects under strong predictor dependence, yielding alternative 2D visualizations that better respect data geometry (Brenning, 2023).

Stability and model-to-model transfer of explanations. A growing line of work studies how sensitive explanations are to perturbations of inputs, parameters, or training conditions, and how consistent they remain across independently trained models. (Agarwal et al., 2022) formalize stability metrics for attribution methods and show that popular saliency techniques can be highly unstable, while (Xue et al., 2023) obtain formal stability guarantees by smoothing the predictor. Algorithmic approaches include training objectives that directly regularize explanation stability (Chen et al., 2024) and VAE-based schemes that generate more stable LIME-style surrogates (Xiang et al., 2023). Beyond single models, (Watson et al., 2022) show that identical architectures with different random seeds can yield markedly different explanations, (Wu et al., 2024) propose an explanation-consistency score between original and adversarial images, and (Rai et al., 2024) quantify consistency of LIME, SHAP, and PDP explanations under varying class-imbalance regimes. These works primarily target local attributions or saliency maps and study stability under perturbations or retraining, whereas we focus on the consistency of *pairwise interaction rankings and ANOVA interaction maps* across independently trained backbones, measured via cross-backbone ranking and surface-alignment metrics.

Evaluating feature interaction explanations. Several recent works explicitly evaluate how well interaction explanations recover known or controlled dependency structure. Examples include grammar-derived dependency relations with rank-based metrics in formal-language classifiers (Jumelet & Zuidema, 2023), Rashomon-set analyses with interaction scores and Halo plots (Li et al., 2023), error-controlled discovery procedures with FDR guarantees on synthetic and semi-synthetic tasks (Chen et al., 2025), and

stability-aware interaction evaluation on industrial intrusion-detection benchmarks (Bouke et al., 2024). XAI-Units and SPEX provide unit-test-style interaction benchmarks and LLM-scale setups with synthetic triggers and downstream QA tasks (Lee et al., 2025; Kang et al., 2025), while complementary work in NLP proposes unified evaluation frameworks for feature explanations with multiple faithfulness and robustness metrics (Sun et al., 2025). In contrast, we develop a targeted evaluation protocol and metrics for global ANOVA interaction maps in regression backbones.

3. Method

3.1. Problem setup and notation

We consider a trained regression backbone $f : \mathcal{X} \subset \mathbb{R}^d \rightarrow \mathbb{R}$, such as a multi-layer perceptron on tabular inputs or a small MLP on latent representations from a vision or language model. Let $X = (X_1, \dots, X_d) \sim P_X$ denote the input random vector and $\{x_i\}_{i=1}^n$ a sample drawn from P_X . Our goal is to construct, for each feature pair (j, k) , a low-dimensional ANOVA interaction map that summarizes how f deviates from additivity in the (X_j, X_k) -plane, together with a scalar interaction strength that can be used for ranking and evaluation. Throughout this section, we treat f and P_X as fixed and focus on how to obtain these objects from black-box evaluations of f on a discretized grid.

3.2. Target: ANOVA interaction map of a backbone

Given a fixed backbone f and input distribution P_X , an ANOVA-style decomposition expresses the response as

$$f(x) = \mu + \sum_{j=1}^d m_j(x_j) + \sum_{1 \leq j < k \leq d} g_{jk}(x_j, x_k) + r(x),$$

where

$$\mu = \mathbb{E}[f(X)], \quad m_j(x_j) = \mathbb{E}[f(X) \mid X_j = x_j] - \mu,$$

and

$$g_{jk}(x_j, x_k) = \mathbb{E}[f(X) \mid X_j = x_j, X_k = x_k] - m_j(x_j) - m_k(x_k) - \mu.$$

is the pairwise interaction component, with $r(x)$ collecting higher-order and residual terms. We refer to g_{jk} as the ANOVA interaction map for the pair (j, k) , and to its L^2 norm

$$S_{jk}^* = \|g_{jk}\|_{L^2(P_{X_j, X_k})}$$

as the corresponding target ANOVA interaction strengths. In practice, directly estimating the conditional expectations in these definitions is infeasible in moderate and high dimensions. Our method therefore fits a discrete factorial surrogate on a grid over \mathcal{X} and recovers approximate ANOVA interaction maps and strengths from this surrogate.

3.3. Discretized factorial surrogate

We first discretize each feature into L bins, inducing a regular grid over \mathcal{X} . For feature j , let $\mathcal{B}_j = \{1, \dots, L\}$ index bins, and let $q_j(x_j) \in \mathcal{B}_j$ denote the bin assignment for value x_j (e.g., via empirical quantiles or uniform spacing over the observed range). A grid point is thus identified by a level vector $\ell = (\ell_1, \dots, \ell_d)$ with $\ell_j \in \mathcal{B}_j$, and we write $f(\ell)$ as shorthand for the backbone prediction at a representative input from that cell.

On this grid, we construct an ANOVA-style linear surrogate

$$\hat{f}_L(\ell) = \hat{\mu} + \sum_{j=1}^d \hat{m}_j(\ell_j) + \sum_{1 \leq j < k \leq d} \hat{g}_{jk}(\ell_j, \ell_k),$$

where $\hat{m}_j : \mathcal{B}_j \rightarrow \mathbb{R}$ and $\hat{g}_{jk} : \mathcal{B}_j \times \mathcal{B}_k \rightarrow \mathbb{R}$ are discrete main-effect and interaction tables. In matrix form, this corresponds to a least-squares fit of a factorial design matrix $\Phi \in \mathbb{R}^{n \times p}$, whose columns encode cell indicators and contrast-coded factors, to the backbone responses $\{f(x_i)\}$. Our framework, ORACLE, solves

$$\hat{\beta} = \arg \min_{\beta} \frac{1}{n} \sum_{i=1}^n (f(x_i) - \langle \beta, \phi(q(x_i)) \rangle)^2,$$

where $\phi(q(x_i))$ denotes the ANOVA basis evaluated at the discretized levels $q(x_i) = (q_1(x_{i1}), \dots, q_d(x_{id}))$. The coefficients $\hat{\beta}$ can then be reshaped into the tables $\hat{\mu}$, $\{\hat{m}_j\}$, and $\{\hat{g}_{jk}\}$.

3.4. Residual centering and μ -rebalancing

A naive least-squares fit in the ANOVA basis does not necessarily enforce the ANOVA identifiability constraints, such as zero-mean main effects and zero row/column sums for interaction tables. To obtain a well-defined decomposition, we apply a simple post-processing step that recenters the estimated tables and rebalances the overall mean.

For each feature j , we subtract the empirical mean of the main-effect table to enforce

$$\sum_{\ell_j \in \mathcal{B}_j} \hat{m}_j(\ell_j) = 0.$$

For each pair (j, k) , we adjust the interaction table \hat{g}_{jk} so that its row and column averages vanish,

$$\sum_{\ell_j} \hat{g}_{jk}(\ell_j, \ell_k) = 0, \quad \sum_{\ell_k} \hat{g}_{jk}(\ell_j, \ell_k) = 0 \quad \text{for all } \ell_j, \ell_k,$$

while preserving the overall mean on the grid. Finally, any constant offset induced by these centering operations is absorbed into $\hat{\mu}$, a step we refer to as μ -rebalancing. After this procedure, the discrete surrogate satisfies

$$\hat{f}_L(\ell) = \hat{\mu} + \sum_{j=1}^d \hat{m}_j(\ell_j) + \sum_{1 \leq j < k \leq d} \hat{g}_{jk}(\ell_j, \ell_k)$$

with the usual ANOVA orthogonality-style constraints at the level of the discretized grid. This makes the main and interaction tables interpretable as discrete approximations of the corresponding ANOVA components of f under P_X . We summarize the centering and μ -rebalancing procedure in Algorithm 1 in Appendix B.

3.5. Extracting ANOVA interaction maps and strengths

The post-processed interaction tables $\hat{g}_{jk} : \mathcal{B}_j \times \mathcal{B}_k \rightarrow \mathbb{R}$ form discrete ANOVA interaction maps for each feature pair (j, k) . These maps can be visualized directly as heatmaps over the (X_j, X_k) grid, revealing regions where the backbone exhibits strong non-additivity. To summarize interaction strength in a single scalar, we compute the root-mean-square (RMS) over the grid,

$$\hat{S}_{jk} = \left(\frac{1}{|\mathcal{B}_j||\mathcal{B}_k|} \sum_{\ell_j \in \mathcal{B}_j} \sum_{\ell_k \in \mathcal{B}_k} \hat{g}_{jk}(\ell_j, \ell_k)^2 \right)^{1/2},$$

and use $\{\hat{S}_{jk}\}_{j < k}$ to rank interactions. In our experiments, these estimated ANOVA interaction maps and strengths serve as the global explanations produced by ORACLE. They are evaluated against oracle ANOVA interaction maps derived from the backbone and P_X , and compared to SHAP-family baselines in terms of interaction selection, hotspot localization, cross-backbone transfer, scale alignment, and intervention-oriented utility.

4. Theory

4.1. Oracle ANOVA interaction decomposition

We view the trained backbone f as a square-integrable function on the input distribution: $X = (X_1, \dots, X_d) \sim P_X$ and $f \in L^2(P_X)$. Following the functional ANOVA literature, we consider a decomposition of $L^2(P_X)$ into mutually orthogonal subspaces

$$L^2(P_X) = \mathcal{H}_0 \oplus \left(\bigoplus_{j=1}^d \mathcal{H}_j \right) \oplus \left(\bigoplus_{1 \leq j < k \leq d} \mathcal{H}_{jk} \right) \oplus \mathcal{R},$$

where \mathcal{H}_0 is the space of constants, \mathcal{H}_j contains main effects of X_j , \mathcal{H}_{jk} contains pairwise interactions between (X_j, X_k) , and \mathcal{R} collects higher-order and residual components.

Definition 4.1 (Oracle ANOVA decomposition). For $f \in L^2(P_X)$, the oracle ANOVA decomposition is

$$f(x) = \mu + \sum_{j=1}^d m_j(x_j) + \sum_{1 \leq j < k \leq d} g_{jk}(x_j, x_k) + r(x),$$

with $\mu \in \mathcal{H}_0$, $m_j \in \mathcal{H}_j$, $g_{jk} \in \mathcal{H}_{jk}$, and $r \in \mathcal{R}$.

Under mild regularity conditions, the ANOVA components admit conditional-expectation representations. In particular, if we define

$$\mu = \mathbb{E}[f(X)], \quad m_j(x_j) = \mathbb{E}[f(X) \mid X_j = x_j] - \mu,$$

then the pairwise terms satisfy

$$g_{jk}(x_j, x_k) = \mathbb{E}[f(X) \mid X_j = x_j, X_k = x_k] - m_j(x_j) - m_k(x_k) - \mu.$$

and this representation coincides with the orthogonal decomposition in Definition 4.1 (see Appendix for details).

Definition 4.2 (Oracle ANOVA interaction map and strength). For each pair (j, k) , we call g_{jk} the *oracle ANOVA interaction map* of (X_j, X_k) , and define the corresponding *target ANOVA interaction strength* as

$$S_{jk}^* = \|g_{jk}\|_{L^2(P_{X_j, X_k})} = \left(\mathbb{E}[g_{jk}(X_j, X_k)^2] \right)^{1/2}.$$

Remark 4.3. The decomposition in Definition 4.1 is formally identical to the classical two-factor ANOVA decomposition used in design-of-experiments: the spaces \mathcal{H}_j and \mathcal{H}_{jk} play the roles of main effects and interaction effects, respectively. The only difference is that we take f to be an arbitrary learned predictor (e.g., a neural network) rather than a linear model, and we work with the data-generating distribution P_X instead of a fixed factorial design.

4.2. ORACLE surrogate as a discrete L^2 projection

We now connect the ORACLE surrogate from Section 3 to the oracle ANOVA decomposition above. Let $q_j : \mathbb{R} \rightarrow \{1, \dots, L\}$ denote the binning map for feature X_j , and define the discretized variables $Z_j = q_j(X_j)$ and $Z = (Z_1, \dots, Z_d) \sim P_Z$. On the discrete grid $\mathcal{B}_j = \{1, \dots, L\}$, we consider the finite-dimensional ANOVA subspaces

$$\mathcal{H}_0^L, \quad \mathcal{H}_j^L, \quad \mathcal{H}_{jk}^L \subset L^2(P_Z),$$

spanned by contrast-coded main-effect and interaction basis functions of Z .

Let $\phi(Z) \in \mathbb{R}^p$ denote the concatenation of basis terms corresponding to \mathcal{H}_0^L , $\{\mathcal{H}_j^L\}$, and $\{\mathcal{H}_{jk}^L\}$. The population version of the ORACLE surrogate solves

$$\beta^* = \arg \min_{\beta} \mathbb{E}[(f(X) - \langle \beta, \phi(Z) \rangle)^2], \quad (1)$$

and we set $f^L(Z) = \langle \beta^*, \phi(Z) \rangle$.

Proposition 4.4 (Discrete ANOVA projection). *The minimizer β^* in Equation (1) exists and is unique under standard conditions, and the corresponding function f^L admits a discrete ANOVA decomposition*

$$f^L(z) = \mu^L + \sum_{j=1}^d m_j^L(z_j) + \sum_{1 \leq j < k \leq d} g_{jk}^L(z_j, z_k),$$

with $\mu^L \in \mathcal{H}_0^L$, $m_j^L \in \mathcal{H}_j^L$, and $g_{jk}^L \in \mathcal{H}_{jk}^L$. Moreover, f^L is the $L^2(P_Z)$ -orthogonal projection of $f(X)$ onto $\mathcal{H}_0^L \oplus (\bigoplus_j \mathcal{H}_j^L) \oplus (\bigoplus_{j < k} \mathcal{H}_{jk}^L)$.

Remark 4.5. The discrete interaction components g_{jk}^L in Proposition 4.4 can be viewed as bin-wise averages of the oracle ANOVA interaction maps g_{jk} within each cell of the grid (Z_j, Z_k) . In this sense, g_{jk}^L is the piecewise-constant L^2 -projection of g_{jk} onto the discretized ANOVA space.

In practice, ORACLE replaces the population expectation in Equation (1) with the empirical average over $\{x_i\}_{i=1}^n$ and solves the resulting least-squares problem to obtain an estimator $\hat{\beta}$. Under standard conditions (e.g., bounded second moments and full-rank design), the estimator is consistent.

Proposition 4.6 (Finite-sample convergence). *Assume the usual regularity conditions for linear regression in the ANOVA basis. Then the least-squares estimator $\hat{\beta}$ converges in probability to β^* as $n \rightarrow \infty$, and the corresponding discrete components satisfy*

$$\|\hat{g}_{jk} - g_{jk}^L\|_2 \xrightarrow{P} 0 \quad \text{for all } 1 \leq j < k \leq d,$$

where the norm is taken over the discrete grid $\mathcal{B}_j \times \mathcal{B}_k$.

4.3. Consistency of interaction strengths and Top- K selection

We now study the behavior of the interaction strengths induced by the discrete ANOVA maps. For a fixed grid size L , define the discrete interaction strength

$$S_{jk}^L = \left(\mathbb{E}[g_{jk}^L(Z_j, Z_k)^2] \right)^{1/2},$$

and its empirical counterpart

$$\hat{S}_{jk} = \left(\frac{1}{|\mathcal{B}_j||\mathcal{B}_k|} \sum_{\ell_j \in \mathcal{B}_j} \sum_{\ell_k \in \mathcal{B}_k} \hat{g}_{jk}(\ell_j, \ell_k)^2 \right)^{1/2}.$$

Theorem 4.7 (Consistency of discrete interaction strengths). *Under the conditions of Proposition 4.6, we have*

$$\hat{S}_{jk} \xrightarrow{P} S_{jk}^L \quad \text{for all } 1 \leq j < k \leq d \quad \text{as } n \rightarrow \infty.$$

If, in addition, the oracle maps g_{jk} are square-integrable and sufficiently regular, then for each (j, k) ,

$$S_{jk}^L \rightarrow S_{jk}^* \quad \text{as } L \rightarrow \infty.$$

We next translate this convergence into guarantees for ranking and NDCG-style metrics. Let $S_{(1)}^* \geq \dots \geq S_{(M)}^*$ denote the sorted oracle strengths over all $M = \binom{d}{2}$ pairs, and similarly let $\hat{S}_{(1)} \geq \dots \geq \hat{S}_{(M)}$ be the sorted estimated strengths.

Theorem 4.8 (Top- K selection consistency). *Suppose there exists a margin $\Delta > 0$ such that*

$$S_{(K)}^* - S_{(K+1)}^* \geq \Delta$$

for some fixed $K \in \{1, \dots, M-1\}$. Then, as $n \rightarrow \infty$ and $L \rightarrow \infty$,

$$\mathbb{P}(\text{Top-}K(\hat{S}_{jk}) = \text{Top-}K(S_{jk}^*)) \rightarrow 1,$$

where $\text{Top-}K(\cdot)$ denotes the set of indices of the K largest entries.

Corollary 4.9 (NDCG@ K consistency). *Under the assumptions of Theorem 4.8, the normalized discounted cumulative gain at K between the estimated and oracle strengths satisfies*

$$\text{NDCG@}K(\hat{S}, S^*) \rightarrow 1 \quad \text{as } n \rightarrow \infty, L \rightarrow \infty.$$

In particular, the NDCG@5 metric used in our experiments is a consistent measure of the ability of ORACLE to recover the top- K target ANOVA interaction strengths.

4.4. Connection to classical 2^5 factorial designs

Finally, we show that in a simple synthetic setting, ORACLE reduces exactly to the classical two-level factorial ANOVA used in design-of-experiments. Consider a setting with $d = 5$ factors, each taking values in $\{-1, +1\}$ with equal probability, and a true response of the form

$$f^*(x) = \beta_0 + \sum_{j=1}^5 \beta_j x_j + \sum_{1 \leq j < k \leq 5} \gamma_{jk} x_j x_k, \quad (2)$$

$$x \in \{-1, +1\}^5.$$

Proposition 4.10 (Homomorphism to classical 2^5 factorial ANOVA). *Suppose the backbone f in Equation (2) is trained to interpolate f^* on all 2^5 design points and we apply ORACLE with $L = 2$ bins per feature, using the standard contrast-coding for $\{-1, +1\}$. Then:*

1. The population design matrix of the ANOVA surrogate coincides with the classical 2^5 full factorial design matrix.
2. The ANOVA surrogate recovers the coefficients of f^* exactly, and the oracle ANOVA interaction maps satisfy

$$g_{jk}(x_j, x_k) = \gamma_{jk} x_j x_k, \quad S_{jk}^* \propto |\gamma_{jk}|.$$

In particular, the ranking of interaction strengths induced by ORACLE is identical to the ranking of the absolute interaction coefficients $|\gamma_{jk}|$ in the underlying factorial model.

Remark 4.11. Proposition 4.10 explains why ORACLE exhibits near-ideal behavior on the 2^5 synthetic experiment in our evaluation: in this home-ground regime, the discrete ANOVA surrogate is algebraically identical to the classical factorial ANOVA design, so that interaction strengths, interaction maps, and cross-backbone stability metrics all align perfectly with the ground truth.

5. Experiments

Datasets. We evaluate interaction explanations on three tabular regression benchmarks. The first is a synthetic 2^5 factorial design with five binary factors $X_j \in \{-1, +1\}$ and a ground-truth response $f^*(x) = \beta_0 + \sum_j \beta_j x_j + \sum_{j < k} \gamma_{jk} x_j x_k$ with a sparse set of large interaction coefficients $\{\gamma_{jk}\}$ that induce a clearly separated Top- K interaction structure. The second benchmark is the UCI Airfoil Self-Noise dataset, a low-dimensional physical regression problem with five continuous inputs and a scalar sound-pressure level target. The third is OpenML kin8nm, a moderately sized nonlinear regression dataset ($N \approx 8,000$, $d \approx 8$). For all datasets we standardize continuous features and use fixed train/validation/test splits.

Model architecture. For each dataset we train two fully connected neural regressors with different capacities. On the synthetic 2^5 benchmark we use small two-layer MLPs; on Airfoil we use two-layer MLPs; and on kin8nm we use three-layer MLPs, with hidden widths between 32 and 256 and light dropout only in the larger Airfoil model. All models are trained with mean-squared error loss using Adam and early stopping on a held-out validation set. After training, the backbones are frozen and all interaction explanations (ORACLE and SHAP-family methods) are computed on these models using the same data splits across multiple random seeds.

Comparison methods. We compare our ANOVA-based interaction framework, **ORACLE**, to five SHAP-family (Shapley-based) interaction estimators. ORACLE is not itself a Shapley-based explainer: it does not rely on coalition sampling or game-theoretic axioms, but instead performs an ANOVA-style orthogonal decomposition on a factorial surrogate of the backbone model (Section 3). Nevertheless, ORACLE and the Shapley-based baselines all aim to quantify the same notion of *global pairwise interaction strength* for each feature pair, which makes them directly comparable in our evaluation. ORACLE fits an ANOVA surrogate on a discretized grid and extracts ANOVA interaction maps and interaction strengths as described in Section 3. As SHAP-based baselines, we include the following methods:

- **FSI**: the Faithful Shapley interaction index, which provides an axiomatic Shapley-based measure of global

interaction strength (Tsai et al., 2023).

- **SHAP-IQ**: a unified Monte Carlo scheme for approximating any-order Shapley interactions (Fumagalli et al., 2023).
- **SVARM-IQ**: an accelerated variant of SHAP-IQ that uses stratified sampling over subset sizes to reduce variance and computation (Kolpaczki et al., 2024).
- **KS-Int**: a KernelSHAP-style weighted least-squares formulation for Shapley interaction indices (Fumagalli et al., 2024).
- **DS-Int**: a DeepSHAP-style multi-reference interaction approximation built on gradient-based attributions (Chen et al., 2020).

All baselines are run with a shared sampling budget and reference/background configuration tailored to each dataset; additional implementation details are provided in the appendix.

Metrics. All methods are evaluated against the oracle ANOVA interaction maps g_{jk} and target ANOVA interaction strengths S_{jk}^* induced by the frozen backbone and data distribution (Section 4). We use five complementary metrics:

- **NDCG@K**: agreement between the ranking induced by estimated strengths \hat{S}_{jk} and the oracle ranking of feature pairs, with emphasis on the top- K interactions.
- **Peak-IoU@q**: spatial overlap between oracle and estimated interaction maps, measured as the intersection-over-union of the top- q fraction of $|g_{jk}|$ and $|\hat{g}_{jk}|$.
- **Xfer-NDCG@K**: cross-backbone stability, computed by scoring the ranking obtained on one backbone against the oracle strengths of the other backbone.
- **CCC**: Lin’s concordance correlation coefficient between $\{\hat{S}_{jk}\}$ and $\{S_{jk}^*\}$ over all pairs, capturing both correlation and scale alignment.
- **IG@K,B**: intervention-oriented utility, defined as the fraction of target ANOVA interaction strengths mass recoverable by selecting up to B pairs among the top- K interactions proposed by a method.

Unless otherwise stated, we use $K = 5$, $q = 0.10$, and $B = 3$, and report all metrics as mean \pm 95% confidence intervals over multiple random seeds.

Results. Figure 1 summarizes mean scores for all five interaction metrics across the three regression benchmarks. For Airfoil, Figure 2 shows that the main-effect curves derived from the ANOVA surrogate match classical DoE-style factor trends, and Figure 3 in Appendix D illustrates localized interaction hotspots, indicating that ORACLE’s ANOVA structure is visually as well as numerically faithful. Across datasets, ORACLE consistently achieves the highest NDCG@K and Xfer-NDCG@K, indicating more accurate recovery of top interaction pairs and more stable rankings across backbones than SHAP-family baselines, and obtains strong Peak-IoU@q and CCC scores, reflecting good hotspot alignment and scale calibration of interaction strengths. For the intervention metric IG@K,B, ORACLE remains competitive with the best SHAP-family methods, suggesting that improved detection and localization do not come at the expense of intervention-oriented utility. Bootstrap confidence intervals in Appendix C corroborate these trends, with gains in NDCG-based and CCC metrics typically exceeding variability across random seeds.

Ablation study. On Airfoil, we ablate the surrogate design and grid resolution of ORACLE. Table 1 compares the full ANOVA surrogate with empirical centering and μ -rebalance to a no-centering variant and a per-pair empirical estimator. All three achieve high detection and transfer scores, reflecting the simplicity of this low-dimensional problem, and the per-pair variant attains slightly higher NDCG@5 and Xfer-NDCG@5, indicating that independent 2D averaging is already near-oracle in this setting. Table 2 varies the grid resolution L and shows that a moderate resolution ($L = 5$) offers the best trade-off between detection and cross-backbone transfer, while overly coarse grids ($L = 3$) improve Peak-IoU by smoothing fine structure and overly fine grids ($L \geq 7$) suffer from bin sparsity and degrade all metrics.

Table 1. Ablation on ORACLE design variants on **Airfoil** (Backbone A/B). We report mean scores over feature pairs for detection (NDCG@5), hotspot overlap (Peak-IoU@0.10), and cross-backbone transfer (Xfer-NDCG@5).

Variant	NDCG@5	Peak-IoU@0.10	Xfer-NDCG@5
Full ORACLE	0.9085	0.2000	0.9555
No-centering	0.9075	0.2333	0.9542
Pairwise-only	0.9864	0.2333	0.9822

6. Discussion and Limitations

Discussion. Across the three tabular regression benchmarks, the ANOVA surrogate consistently recovered the backbone’s top interaction structure more accurately than SHAP-family interaction estimators: ORACLE attains higher NDCG@5 and Xfer-NDCG@5 in nearly all settings, together with strong Peak-IoU@0.10 and CCC, indicating

Table 2. Ablation on grid resolution L for ORACLE on Airfoil (Backbone A/B). We report detection (NDCG@5), hotspot overlap (Peak-IoU@0.10), and cross-backbone transfer (Xfer-NDCG@5) as L varies.

L	NDCG@5	Peak-IoU@0.10	Xfer-NDCG@5
3	0.9065	0.3000	0.9100
5	0.9802	0.2300	0.9735
7	0.8754	0.1675	0.8860
9	0.8532	0.0921	0.8427

better agreement with target ANOVA interaction strengths, more stable rankings across independently trained backbones, and well-localized, scale-calibrated detection of interaction hotspots. Beyond these scalar metrics, Figure 2 shows that the recovered main-effect curves match classical DoE-style factor trends, and Figure 3 in Appendix D reveals localized hotspots aligned with the detected top pairs, suggesting that the learned ANOVA structure is visually as well as numerically faithful. The intervention metric IG@K,B is more mixed: SHAP-family methods sometimes achieve similar or slightly higher IG, consistent with their game-theoretic design as marginal contribution scores tailored to removal-style interventions, whereas ORACLE is explicitly optimized for L^2 fidelity and variance decomposition and therefore yields its largest advantages on the synthetic 2^5 factorial design, with still robust gains on Airfoil and kin8nm, indicating that moderately complex tabular predictors admit low-order ANOVA projections that are faithful enough for interaction benchmarking. As a complementary case study, the latent image and text experiments in Appendix E show that grid-based ANOVA surrogates are less competitive in highly entangled latent spaces, reinforcing that ORACLE is best suited to settings where features admit interpretable factorial structure.

Limitations. ORACLE inherits several limitations from its ANOVA and grid-based design. First, interaction maps are defined on a discretized input grid, so performance depends on binning and can suffer when many features or high resolutions lead to sparse cells; our ablation on the grid size L suggests that moderate grids (e.g., $L \in \{3, 5, 7\}$) offer a reasonable trade-off between resolution and stability. Second, we restrict attention to pairwise interactions in regression backbones and treat the ANOVA decomposition of the trained model under the observed data distribution as the target, so higher-order effects or severe model misspecification can make these targets misaligned with domain notions of interaction. Third, SHAP baselines are evaluated under a fixed Monte Carlo budget and shared reference configuration, and alternative sampling schemes or background choices might improve their metrics and narrow the observed gaps. Finally, our main results focus on

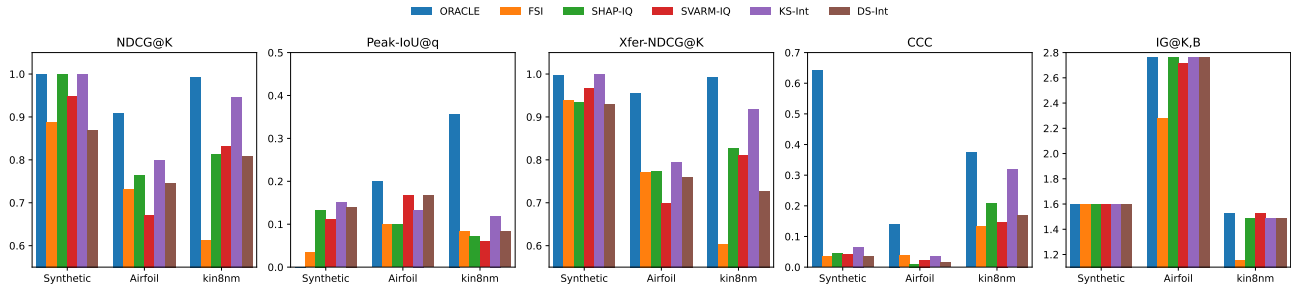


Figure 1. Grouped bar plots of mean interaction metrics across datasets. Each panel shows one metric (NDCG@K, Peak-IoU@q, Xfer-NDCG@K, CCC, IG@K,B with $K = 5$, $q = 0.10$, $B = 3$); within each dataset, bars compare ORACLE to SHAP-family interaction methods. Higher values indicate better interaction detection, localization, transfer, scale agreement, or intervention utility.

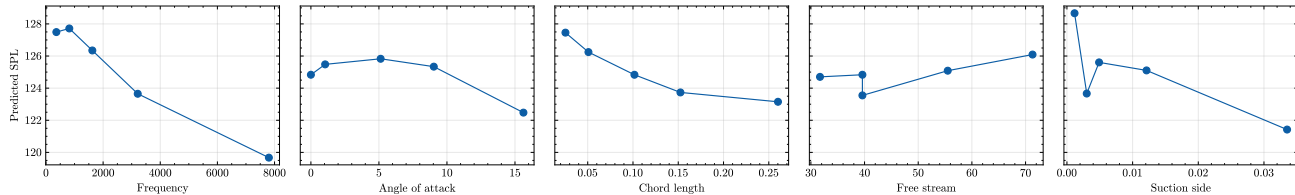


Figure 2. Classical ORACLE main-effect plots for the Airfoil dataset (Backbone A). Each panel shows the marginal response $\mu + m_j(x_j)$ as a function of the bin centers for feature j , with all other features integrated out under the empirical input distribution.

low- to medium-dimensional tabular tasks and MLP architectures, so the conclusions may not directly transfer to high-dimensional vision or language models with strong local structure or entangled latent representations.

Future work. Several extensions follow naturally from these observations. Methodologically, scaling ANOVA surrogates beyond low- to medium-dimensional tabular data will likely require adaptive or sparse grids with local refinement of interaction hotspots and structured bases that better respect feature correlations, as well as extensions to classification, sequence, graph backbones, and higher-order interaction maps. On the evaluation side, combining oracle-based metrics with additional stability and robustness criteria under distribution shift, alternative training runs, or architectural changes could yield more comprehensive interaction benchmarks. Finally, closer integration with SHAP-style estimators—for example, using ANOVA maps as priors, sanity checks, or guides for targeted Monte Carlo sampling—may lead to hybrid methods that combine the structured semantics of design-of-experiments with the flexibility of Shapley-based interaction indices.

7. Conclusion

This work introduced ORACLE, an ANOVA-based framework for explaining feature interactions in neural network regressors. By treating a trained predictor as a target and fitting an orthogonal surrogate, the method produces interaction tables and maps that are directly tied to the model’s

non-additive structure. Empirical results across controlled and realistic settings indicate that these ANOVA-style surrogates can offer more faithful, stable, and interpretable views of interactions than existing Shapley-based approaches, especially on tabular domains where design-of-experiments intuitions apply. Overall, the framework provides a principled bridge between classical ANOVA and modern deep learning, and it lays a foundation for future extensions to richer architectures, data modalities, and hybrid interaction explainers.

Impact Statement

This work proposes an ANOVA-based framework for explaining feature interactions in neural network regressors and for systematically evaluating interaction explanation methods. By grounding interaction maps in an orthogonal surrogate fitted to a trained predictor, the framework aims to give practitioners a more faithful and stable view of how pairs of features jointly influence model outputs, which can benefit experimental design, engineering, and scientific modeling where understanding synergistic and antagonistic effects between factors is central. The accompanying evaluation protocol may also help the research community compare interaction methods more rigorously, clarifying when different explanation families are reliable and when they diverge.

However, the framework does not turn black-box models into causal instruments or guarantee that learned interactions reflect ground-truth mechanisms. Visually appealing inter-

action maps could be over-trusted, used to justify biased or misspecified models, or presented as causal evidence in sensitive domains such as healthcare or policy. Our experiments rely on standard public regression benchmarks and do not directly involve personal or sensitive data, but the methodology itself can be applied more broadly. We therefore encourage users to treat these explanations as one diagnostic among many, to combine them with domain knowledge and robustness checks, and to exercise particular caution in high-stakes settings or when reasoning about fairness, accountability, or causal claims.

References

- Agarwal, C., Johnson, N., Pawelczyk, M., Krishna, S., Saxena, E., Zitnik, M., and Lakkaraju, H. Rethinking stability for attribution-based explanations. *arXiv preprint arXiv:2203.06877*, 2022.
- Bouke, M. A., Abdullah, A., Cengiz, K., and Akleyek, S. Application of bukagini algorithm for enhanced feature interaction analysis in intrusion detection systems. *PeerJ Computer Science*, 10:e2043, 2024.
- Brenning, A. Interpreting machine-learning models in transformed feature space with an application to remote-sensing classification. *Machine Learning*, 112(9):3455–3471, 2023.
- Chen, C., Guo, C., Chen, R., Ma, G., Zeng, M., Liao, X., Zhang, X., and Xie, S. Training for stable explanation for free. *Advances in Neural Information Processing Systems*, 37:3421–3457, 2024.
- Chen, H., Lundberg, S., and Lee, S.-I. Explaining models by propagating shapley values of local components. In *Explainable AI in Healthcare and Medicine: Building a Culture of Transparency and Accountability*, pp. 261–270. Springer, 2020.
- Chen, W., Jiang, Y., Noble, W. S., and Lu, Y. Y. Error-controlled non-additive interaction discovery in machine learning models. *Nature Machine Intelligence*, pp. 1–14, 2025.
- Choi, Y., Park, S., Park, C., Kim, D., and Kim, Y. Meta-anova: screening interactions for interpretable machine learning. *Journal of the Korean Statistical Society*, pp. 1–18, 2025.
- Dolar, T., Lee, D., and Chen, W. Data-driven global sensitivity analysis of variable groups for understanding complex physical interactions in engineering design. *Journal of Mechanical Design*, 146(9), 2024.
- Fontana, R., Molena, A., Pegoraro, L., and Salmaso, L. Design of experiments and machine learning with application to industrial experiments. *Statistical Papers*, 64(4): 1251–1274, 2023.
- Fumagalli, F., Muschalik, M., Kolpaczki, P., Hüllermeier, E., and Hammer, B. Shap-iq: Unified approximation of any-order shapley interactions. *Advances in Neural Information Processing Systems*, 36:11515–11551, 2023.
- Fumagalli, F., Muschalik, M., Kolpaczki, P., Hüllermeier, E., and Hammer, B. Kernelshap-iq: Weighted least-square optimization for shapley interactions. *arXiv preprint arXiv:2405.10852*, 2024.
- Gkolemis, V., Dalamagas, T., and Diou, C. Dale: Differential accumulated local effects for efficient and accurate global explanations. In *Asian Conference on Machine Learning*, pp. 375–390. PMLR, 2023.
- Gkolemis, V., Dalamagas, T., Ntoutsis, E., and Diou, C. Fast and accurate regional effect plots for automated tabular data analysis. *Proceedings of the VLDB Endowment*. ISSN, 2150:8097, 2024a.
- Gkolemis, V., Diou, C., Ntoutsis, E., Dalamagas, T., Bischl, B., Herbringer, J., and Casalicchio, G. Effector: A python package for regional explanations. *arXiv preprint arXiv:2404.02629*, 2024b.
- Herbringer, J., Bischl, B., and Casalicchio, G. Repid: Regional effect plots with implicit interaction detection. In *International conference on artificial intelligence and statistics*, pp. 10209–10233. PMLR, 2022.
- Herbringer, J., Wright, M. N., Nagler, T., Bischl, B., and Casalicchio, G. Decomposing global feature effects based on feature interactions. *Journal of Machine Learning Research*, 25(381):1–65, 2024.
- Hu, L., Nair, V. N., Sudjianto, A., Zhang, A., Chen, J., and Yang, Z. Interpretable machine learning based on functional anova framework: algorithms and comparisons. *Applied Stochastic Models in Business and Industry*, 41 (1):e2916, 2025.
- Inglis, A., Parnell, A., and Hurley, C. B. Visualizing variable importance and variable interaction effects in machine learning models. *Journal of Computational and Graphical Statistics*, 31(3):766–778, 2022.
- Jumelet, J. and Zuidema, W. Feature interactions reveal linguistic structure in language models. *arXiv preprint arXiv:2306.12181*, 2023.
- Kang, J. S., Butler, L., Agarwal, A., Erginbas, Y. E., Pedarsani, R., Ramchandran, K., and Yu, B. Spex: Scaling feature interaction explanations for llms. *arXiv preprint arXiv:2502.13870*, 2025.

- Kerrigan, D., Barr, B., and Bertini, E. Pdpilot: Exploring partial dependence plots through ranking, filtering, and clustering. *IEEE Transactions on Visualization and Computer Graphics*, 2025.
- Köhler, D., Rügamer, D., Boyle, L. J., Maloney, K. O., and Schmid, M. Achieving interpretable machine learning by functional decomposition of black-box models into explainable predictor effects. *npj Artificial Intelligence*, 1(1):34, 2025.
- Kolpaczki, P., Muschalik, M., Fumagalli, F., Hammer, B., and Hüllermeier, E. Svrm-iq: Efficient approximation of any-order shapley interactions through stratification. *arXiv preprint arXiv:2401.13371*, 2024.
- Lee, J. R., Emami, S., Hollins, M. D., Wong, T. C., Villalobos Sánchez, C. I., Toni, F., Zhang, D., and Dejl, A. Xai-units: Benchmarking explainability methods with unit tests. In *Proceedings of the 2025 ACM Conference on Fairness, Accountability, and Transparency*, pp. 2892–2905, 2025.
- Li, S., Wang, R., Deng, Q., and Barnard, A. Exploring the cloud of feature interaction scores in a rashomon set. *arXiv preprint arXiv:2305.10181*, 2023.
- Muschalik, M., Baniecki, H., Fumagalli, F., Kolpaczki, P., Hammer, B., and Hüllermeier, E. shapiq: Shapley interactions for machine learning. *Advances in Neural Information Processing Systems*, 37:130324–130357, 2024.
- Park, S., Kong, I., Choi, Y., Park, C., and Kim, Y. Tensor product neural networks for functional anova model. *arXiv preprint arXiv:2502.15215*, 2025.
- Rai, T., He, J., Kaur, J., Shen, Y., Mahmud, M., Brown, D. J., O’Dowd, E., and Baldwin, D. Evaluating xai techniques under class imbalance using cprd data. *Frontiers in Artificial Intelligence*, 8:1682919, 2024.
- Singhvi, D., Erkelens, A., Jain, R., Misra, D., and Saphra, N. Knowing your nonlinearities: Shapley interactions reveal the underlying structure of data. *arXiv e-prints*, pp. arXiv–2403, 2024.
- Sun, J., Atanasova, P., and Augenstein, I. Evaluating input feature explanations through a unified diagnostic evaluation framework. In *Proceedings of the 2025 Conference of the Nations of the Americas Chapter of the Association for Computational Linguistics: Human Language Technologies (Volume 1: Long Papers)*, pp. 10559–10577, 2025.
- Tsai, C.-P., Yeh, C.-K., and Ravikumar, P. Faith-shap: The faithful shapley interaction index. *Journal of Machine Learning Research*, 24(94):1–42, 2023.
- Watson, M., Hasan, B. A. S., and Al Moubayed, N. Agree to disagree: When deep learning models with identical architectures produce distinct explanations. In *Proceedings of the IEEE/CVF Winter Conference on Applications of Computer Vision*, pp. 875–884, 2022.
- Wu, H., Jiang, H., Wang, K., Tang, Z., He, X., and Lin, L. Improving network interpretability via explanation consistency evaluation. *IEEE Transactions on Multimedia*, 2024.
- Xiang, X., Yu, H., Wang, Y., and Wang, G. Stable local interpretable model-agnostic explanations based on a variational autoencoder. *Applied Intelligence*, 53(23): 28226–28240, 2023.
- Xue, A., Alur, R., and Wong, E. Stability guarantees for feature attributions with multiplicative smoothing. *Advances in Neural Information Processing Systems*, 36: 62388–62413, 2023.
- Zubair, S. W. H., Arafat, S. M., Khan, S. A., Niazi, S. G., Rehan, M., Arshad, M. U., Hayat, N., Aized, T., Uddin, G. M., and Riaz, F. Coupling taguchi experimental designs with deep adaptive learning enhanced ai process models for experimental cost savings in manufacturing process development. *Scientific Reports*, 14(1):23428, 2024.

A. Proofs and Additional Theoretical Details

A.1. Additional assumptions and notation

We collect here the probabilistic setting, basic notation, and additional assumptions used in the theoretical results of the main text.

Basic setup. Let $X = (X_1, \dots, X_d)$ be a random vector taking values in a measurable space $\mathcal{X} \subseteq \mathbb{R}^d$, with distribution P_X . We denote by P_{X_j} and P_{X_j, X_k} the marginals of X_j and (X_j, X_k) . A trained predictor is a measurable function

$$f : \mathcal{X} \rightarrow \mathbb{R},$$

which we treat as fixed throughout the analysis (conditioning on the training procedure). We write

$$\mu := \mathbb{E}[f(X)]$$

for the global mean under P_X .

Assumption A.1 (Square-integrable predictor). The predictor f is square-integrable with respect to P_X , i.e. $f \in L^2(P_X)$ and $\mathbb{E}[f(X)^2] < \infty$.

Function spaces and inner products. For any random vector U with distribution P_U , we define

$$L^2(P_U) := \{h : \text{supp}(P_U) \rightarrow \mathbb{R} \mid \mathbb{E}[h(U)^2] < \infty\}.$$

We equip $L^2(P_U)$ with the inner product

$$\langle h_1, h_2 \rangle_{L^2(P_U)} := \mathbb{E}[h_1(U) h_2(U)]$$

and norm $\|h\|_{L^2(P_U)} := \sqrt{\langle h, h \rangle_{L^2(P_U)}}$. When the underlying distribution is clear from the context, we abbreviate $\langle \cdot, \cdot \rangle$ and $\|\cdot\|_2$.

In particular, for each feature j and feature pair (j, k) , we will use

$$L^2(P_{X_j}), \quad L^2(P_{X_j, X_k})$$

for main-effect and pairwise interaction components, respectively.

Assumption A.2 (Regular conditional expectations). For any subset of coordinates of X , regular conditional distributions exist, so that $\mathbb{E}[f(X) \mid X_j = x_j]$ and $\mathbb{E}[f(X) \mid X_j = x_j, X_k = x_k]$ are well-defined for P_{X_j} - and P_{X_j, X_k} -almost every (x_j, x_k) .

Under Assumptions A.1–A.2, the oracle main and pairwise components in the main text can be written as

$$m_j(x_j) := \mathbb{E}[f(X) \mid X_j = x_j] - \mu, \quad m_{jk}(x_j, x_k) := \mathbb{E}[f(X) \mid X_j = x_j, X_k = x_k] - \mu,$$

and the oracle non-additive residual surface

$$g_{jk}(x_j, x_k) := m_{jk}(x_j, x_k) - m_j(x_j) - m_k(x_k) + \mu$$

is an element of $L^2(P_{X_j, X_k})$ for each pair (j, k) .

target ANOVA interaction strength. For each pair (j, k) , we define the target ANOVA interaction strength

$$S_{jk}^* := \|g_{jk}\|_{L^2(P_{X_j, X_k})} = \left(\mathbb{E}[g_{jk}(X_j, X_k)^2] \right)^{1/2}.$$

This quantity is used as the ground-truth score in the ranking-based metrics (NDCG@K, Xfer-NDCG@K) in the main text.

Discretization and quantization. For each feature $j \in \{1, \dots, d\}$, let

$$q_j : \mathbb{R} \rightarrow \{1, \dots, L_j\}$$

be a fixed quantization map that assigns each value of X_j to one of L_j bins. We denote the discretized covariates by

$$Z_j := q_j(X_j), \quad Z := (Z_1, \dots, Z_d),$$

and write P_Z for the distribution of Z . For simplicity in the theoretical results we often assume $L_j = L$ for all j , so that $Z_j \in \{1, \dots, L\}$ and $Z \in \{1, \dots, L\}^d$.

For a given pair (j, k) , the corresponding two-dimensional grid of bins is

$$\mathcal{G}_{jk} := \{1, \dots, L\} \times \{1, \dots, L\},$$

and a binned interaction surface can be viewed as a function $g_{jk}^L : \mathcal{G}_{jk} \rightarrow \mathbb{R}$.

ANOVA basis and design matrix. The ANOVA surrogate operates on the discrete variables Z through a collection of basis functions

$$\phi = (\phi_0, \{\phi_j\}_{j=1}^d, \{\phi_{jk}\}_{1 \leq j < k \leq d}),$$

where

- $\phi_0(Z) \equiv 1$ is the intercept term,
- for each j , the main-effect basis $\phi_j(Z)$ only depends on Z_j and is centered so that $\mathbb{E}[\phi_j(Z)] = 0$,
- for each pair (j, k) , the interaction basis $\phi_{jk}(Z)$ only depends on (Z_j, Z_k) and is centered so that $\mathbb{E}[\phi_{jk}(Z) | Z_j] = \mathbb{E}[\phi_{jk}(Z) | Z_k] = 0$.

Given a sample $\{Z_i\}_{i=1}^n$, we write

$$\Phi \in \mathbb{R}^{n \times p}$$

for the corresponding design matrix obtained by evaluating ϕ on each Z_i , and p denotes the total number of ANOVA coefficients (intercept, main effects, and pairwise interactions). This compact notation is used in the proofs of the projection and consistency results in the subsequent subsections.

A.2. Oracle ANOVA decomposition: existence and representation

In this subsection we make explicit how the oracle main and interaction components arise from an ANOVA-style orthogonal decomposition in $L^2(P_X)$.

ANOVA subspaces. Recall the basic setup in Appendix A.1: $X = (X_1, \dots, X_d) \sim P_X$, a fixed predictor $f \in L^2(P_X)$, and $\mu = \mathbb{E}[f(X)]$. We define the following subspaces of $L^2(P_X)$:

$$\begin{aligned} H_0 &:= \{h(X) \equiv c : c \in \mathbb{R}\}, \\ H_j &:= \{h(X) = h_j(X_j) : h_j \in L^2(P_{X_j}), \mathbb{E}[h_j(X_j)] = 0\}, \quad j = 1, \dots, d, \\ H_{jk} &:= \left\{ h(X) = h_{jk}(X_j, X_k) : h_{jk} \in L^2(P_{X_j, X_k}), \mathbb{E}[h_{jk} | X_j] = \mathbb{E}[h_{jk} | X_k] = 0 \right\}, \\ &\quad 1 \leq j < k \leq d. \end{aligned}$$

We also write

$$\mathcal{H}_{\leq 2} := H_0 \oplus \left(\bigoplus_{j=1}^d H_j \right) \oplus \left(\bigoplus_{1 \leq j < k \leq d} H_{jk} \right)$$

for the direct sum of constant, main-effect, and pairwise interaction subspaces, and define the residual subspace as the orthogonal complement

$$R := \mathcal{H}_{\leq 2}^\perp = \{r \in L^2(P_X) : \langle r, h \rangle_{L^2(P_X)} = 0 \ \forall h \in \mathcal{H}_{\leq 2}\}.$$

Lemma A.3 (Orthogonality of ANOVA subspaces). *Under Assumptions A.1–A.2, the subspaces H_0 , $\{H_j\}_{j=1}^d$, and $\{H_{jk}\}_{1 \leq j < k \leq d}$ are pairwise orthogonal in $L^2(P_X)$, and $\mathcal{H}_{\leq 2}$ is a closed subspace of $L^2(P_X)$.*

Proof. We sketch the argument. Orthogonality of H_0 and each H_j, H_{jk} follows from the centering conditions $\mathbb{E}[h_j(X_j)] = 0$ and $\mathbb{E}[h_{jk}(X_j, X_k)] = 0$. For H_j and H_ℓ with $j \neq \ell$,

$$\mathbb{E}[h_j(X_j)h_\ell(X_\ell)] = \mathbb{E}[h_j(X_j) \mathbb{E}[h_\ell(X_\ell) | X_j]] = \mathbb{E}[h_j(X_j) \cdot 0] = 0.$$

Similarly, for H_j and $H_{k\ell}$, conditioning on X_j or (X_k, X_ℓ) and using the defining constraints $\mathbb{E}[h_{k\ell} | X_k] = \mathbb{E}[h_{k\ell} | X_\ell] = 0$ shows that the inner product vanishes. The same tower-property argument applies to H_{jk} and $H_{k\ell}$, H_{jk} and $H_{j\ell}$, and H_{jk} and H_{mn} for distinct pairs (j, k) and (m, n) . Closedness follows from the fact that each subspace is defined by linear constraints expressed in terms of (continuous) conditional expectation operators on L^2 , which preserve closedness. \square

Oracle ANOVA representation. We now show that the oracle main and pairwise components used in the main text correspond to the projections of f onto these subspaces.

Proposition A.4 (Oracle ANOVA decomposition). *Under Assumptions A.1–A.2, define*

$$\begin{aligned} \mu &:= \mathbb{E}[f(X)], \\ m_j(x_j) &:= \mathbb{E}[f(X) | X_j = x_j] - \mu, \quad j = 1, \dots, d, \\ m_{jk}(x_j, x_k) &:= \mathbb{E}[f(X) | X_j = x_j, X_k = x_k] - \mu, \quad 1 \leq j < k \leq d, \\ g_{jk}(x_j, x_k) &:= m_{jk}(x_j, x_k) - m_j(x_j) - m_k(x_k) + \mu, \\ r(x) &:= f(x) - \mu - \sum_{j=1}^d m_j(x_j) - \sum_{1 \leq j < k \leq d} g_{jk}(x_j, x_k). \end{aligned}$$

Then the following hold:

1. $m_j(X_j) \in H_j$ and $g_{jk}(X_j, X_k) \in H_{jk}$ for all j and $j < k$.
2. $r \in R$, i.e. r is orthogonal to H_0 , all H_j , and all H_{jk} .
3. f admits the orthogonal ANOVA-style decomposition

$$f(X) = \mu + \sum_{j=1}^d m_j(X_j) + \sum_{1 \leq j < k \leq d} g_{jk}(X_j, X_k) + r(X),$$

with $\mu \in H_0$, $m_j(X_j) \in H_j$, $g_{jk}(X_j, X_k) \in H_{jk}$, and $r \in R$.

4. This decomposition is unique in the sense that if

$$f(X) = \tilde{\mu} + \sum_{j=1}^d \tilde{m}_j(X_j) + \sum_{1 \leq j < k \leq d} \tilde{g}_{jk}(X_j, X_k) + \tilde{r}(X)$$

with $\tilde{\mu} \in H_0$, $\tilde{m}_j \in H_j$, $\tilde{g}_{jk} \in H_{jk}$, and $\tilde{r} \in R$, then $\tilde{\mu} = \mu$, $\tilde{m}_j = m_j$, $\tilde{g}_{jk} = g_{jk}$, and $\tilde{r} = r$ almost surely.

Proof of (1). For each j ,

$$\mathbb{E}[m_j(X_j)] = \mathbb{E}[\mathbb{E}[f(X) | X_j] - \mu] = \mathbb{E}[f(X)] - \mu = 0,$$

so $m_j(X_j)$ is centered and depends only on X_j , hence $m_j(X_j) \in H_j$. For g_{jk} , note first that

$$\mathbb{E}[g_{jk}(X_j, X_k)] = \mathbb{E}[m_{jk}(X_j, X_k)] - \mathbb{E}[m_j(X_j)] - \mathbb{E}[m_k(X_k)] + \mu = 0,$$

and

$$\begin{aligned} \mathbb{E}[g_{jk}(X_j, X_k) | X_j] &= \mathbb{E}[m_{jk}(X_j, X_k) | X_j] - m_j(X_j) - \mathbb{E}[m_k(X_k) | X_j] + \mu \\ &= (\mathbb{E}[f(X) | X_j] - \mu) - m_j(X_j) - (\mathbb{E}[f(X) | X_j] - \mu) + \mu \\ &= 0, \end{aligned}$$

and symmetrically $\mathbb{E}[g_{jk}(X_j, X_k) | X_k] = 0$. Thus $g_{jk}(X_j, X_k) \in H_{jk}$, proving (1). \square

Proof of (2). Orthogonality of r to H_0 , the H_j , and the H_{jk} follows from the tower property of conditional expectation and the defining constraints in (1). For example,

$$\mathbb{E}[r(X)] = \mathbb{E}[f(X)] - \mu - \sum_j \mathbb{E}[m_j(X_j)] - \sum_{j < k} \mathbb{E}[g_{jk}(X_j, X_k)] = 0,$$

so r is orthogonal to H_0 . For any $h_j(X) = h_j(X_j) \in H_j$,

$$\begin{aligned} \mathbb{E}[r(X)h_j(X_j)] &= \mathbb{E}[f(X)h_j(X_j)] - \mu \mathbb{E}[h_j(X_j)] - \sum_{\ell} \mathbb{E}[m_{\ell}(X_{\ell})h_j(X_j)] \\ &\quad - \sum_{k < \ell} \mathbb{E}[g_{k\ell}(X_k, X_{\ell})h_j(X_j)]. \end{aligned}$$

The second term vanishes since h_j is centered. The third term vanishes for $\ell \neq j$ by the same conditioning argument as in Lemma A.3, and for $\ell = j$ by the definition of m_j as a centered conditional expectation. The fourth term vanishes by conditioning on (X_k, X_{ℓ}) and using the constraints defining $H_{k\ell}$ together with the fact that h_j depends only on X_j . An analogous argument shows orthogonality to each H_{jk} , which proves (2). \square

Proof of (3). The stated decomposition is simply the definition of r :

$$r(x) = f(x) - \mu - \sum_{j=1}^d m_j(x_j) - \sum_{1 \leq j < k \leq d} g_{jk}(x_j, x_k).$$

Parts (1) and (2) show that $\mu \in H_0$, $m_j(X_j) \in H_j$, $g_{jk}(X_j, X_k) \in H_{jk}$, and $r \in R$, so f is written as an orthogonal sum of elements from H_0 , $\{H_j\}$, $\{H_{jk}\}$, and R . This establishes (3). \square

Proof of (4). Suppose we have another decomposition with $\tilde{\mu} \in H_0$, $\tilde{m}_j \in H_j$, $\tilde{g}_{jk} \in H_{jk}$, and $\tilde{r} \in R$:

$$f(X) = \tilde{\mu} + \sum_j \tilde{m}_j(X_j) + \sum_{j < k} \tilde{g}_{jk}(X_j, X_k) + \tilde{r}(X).$$

Subtracting the two representations gives

$$0 = (\mu - \tilde{\mu}) + \sum_j (m_j(X_j) - \tilde{m}_j(X_j)) + \sum_{j < k} (g_{jk}(X_j, X_k) - \tilde{g}_{jk}(X_j, X_k)) + (r(X) - \tilde{r}(X)).$$

By Lemma A.3, the summands belong to mutually orthogonal subspaces H_0 , $\{H_j\}$, $\{H_{jk}\}$, and R , so each term must be zero almost surely. This implies $\mu = \tilde{\mu}$, $m_j = \tilde{m}_j$, $g_{jk} = \tilde{g}_{jk}$, and $r = \tilde{r}$ almost surely, establishing uniqueness and proving (4). \square

Remark A.5 (Connection to classical two-way ANOVA). The decomposition in Proposition A.4 is formally analogous to the standard two-way ANOVA decomposition in designed experiments. In the classical setting, f is a linear model on a finite 2^d factorial design, and the components in H_0 , H_j , and H_{jk} correspond to the intercept, main effects, and interaction contrasts of the design matrix. Here, we work in the Hilbert space $L^2(P_X)$ of an arbitrary trained predictor f , and the same structure arises from orthogonal projection onto the subspaces of functions depending on at most two coordinates with appropriate centering constraints.

A.3. Discrete ANOVA surrogate as an L^2 projection

We now formalize the population-level ANOVA surrogate obtained after discretizing the inputs and show that it coincides with an L^2 projection of the predictor onto a finite-dimensional ANOVA subspace.

Finite-dimensional ANOVA subspace. Recall the discretized variables $Z = (Z_1, \dots, Z_d)$ and the ANOVA basis

$$\phi(Z) = (\phi_0(Z), \{\phi_j(Z)\}_{j=1}^d, \{\phi_{jk}(Z)\}_{1 \leq j < k \leq d}) \in \mathbb{R}^p,$$

where $\phi_0(Z) \equiv 1$, $\phi_j(Z)$ depends only on Z_j and is centered, and $\phi_{jk}(Z)$ depends only on (Z_j, Z_k) and satisfies the centering constraints in Appendix A.1. We write

$$\mathcal{V}_L := \{\beta^\top \phi(Z) : \beta \in \mathbb{R}^p\} \subseteq L^2(P_Z)$$

for the corresponding finite-dimensional subspace of square-integrable functions of Z . Since Z is a deterministic function of X , we can also view any element of \mathcal{V}_L as a function of X via $h(X) := h(Z) = h(q(X))$, so \mathcal{V}_L is a closed finite-dimensional subspace of $L^2(P_X)$ as well.

Assumption A.6 (Nondegenerate ANOVA design). The Gram matrix

$$G := \mathbb{E}[\phi(Z) \phi(Z)^\top] \in \mathbb{R}^{p \times p}$$

is positive definite.

Assumption A.6 rules out redundant basis functions and ensures that the parametrization of \mathcal{V}_L by $\beta \in \mathbb{R}^p$ is well-defined.

Population projection. We consider the population risk

$$J(\beta) := \mathbb{E}[(f(X) - \beta^\top \phi(Z))^2], \quad \beta \in \mathbb{R}^p,$$

and define the population ANOVA surrogate as the minimizer of J .

Proposition A.7 (Discrete ANOVA surrogate as an L^2 projection). *Under Assumptions A.1, A.2, and A.6, the quadratic functional J admits a unique minimizer*

$$\beta^* = \arg \min_{\beta \in \mathbb{R}^p} \mathbb{E}[(f(X) - \beta^\top \phi(Z))^2],$$

given in closed form by

$$\beta^* = G^{-1}b, \quad G := \mathbb{E}[\phi(Z) \phi(Z)^\top], \quad b := \mathbb{E}[\phi(Z) f(X)].$$

The corresponding predictor

$$f_L(Z) := \beta^{*\top} \phi(Z)$$

is the $L^2(P_X)$ -orthogonal projection of $f(X)$ onto the subspace \mathcal{V}_L , i.e.

$$f_L = \arg \min_{g \in \mathcal{V}_L} \mathbb{E}[(f(X) - g(Z))^2],$$

and the residual $f(X) - f_L(Z)$ is orthogonal to \mathcal{V}_L :

$$\mathbb{E}[(f(X) - f_L(Z))g(Z)] = 0 \quad \text{for all } g \in \mathcal{V}_L.$$

Proof. Quadratic expansion of J gives

$$J(\beta) = \mathbb{E}[f(X)^2] - 2\beta^\top \mathbb{E}[\phi(Z) f(X)] + \beta^\top \mathbb{E}[\phi(Z) \phi(Z)^\top] \beta = c - 2\beta^\top b + \beta^\top G \beta,$$

for a constant $c = \mathbb{E}[f(X)^2]$ independent of β . Assumption A.6 implies that G is positive definite, so J is strictly convex and its unique minimizer is characterized by the normal equations

$$\nabla_\beta J(\beta) = -2b + 2G\beta = 0 \quad \implies \quad \beta^* = G^{-1}b.$$

The function $f_L(Z) = \beta^{*\top} \phi(Z)$ lies in \mathcal{V}_L by construction. Conversely, any $g \in \mathcal{V}_L$ can be written as $g(Z) = \gamma^\top \phi(Z)$ for some $\gamma \in \mathbb{R}^p$, and

$$\mathbb{E}[(f(X) - f_L(Z))g(Z)] = \mathbb{E}[(f(X) - \beta^{*\top} \phi(Z)) \gamma^\top \phi(Z)] = \gamma^\top (b - G\beta^*) = 0,$$

since $G\beta^* = b$. Thus f_L is orthogonal to \mathcal{V}_L in the sense of the projection residual, and by the standard Hilbert-space theory of least-squares projections, f_L is the unique $L^2(P_X)$ -projection of f onto \mathcal{V}_L . \square

Discrete ANOVA components. The coefficient vector β^* can be grouped into an intercept, main-effect, and pairwise-interaction blocks,

$$\beta^* = (\beta_0^*, \{\beta_j^*\}_{j=1}^d, \{\beta_{jk}^*\}_{1 \leq j < k \leq d}),$$

so that

$$f_L(Z) = \beta_0^* + \sum_{j=1}^d \phi_j(Z)^\top \beta_j^* + \sum_{1 \leq j < k \leq d} \phi_{jk}(Z)^\top \beta_{jk}^*.$$

By construction of the basis, β_0^* is the discrete intercept, the terms $\phi_j(Z)^\top \beta_j^*$ are centered functions of Z_j , and the terms $\phi_{jk}(Z)^\top \beta_{jk}^*$ are centered functions of (Z_j, Z_k) satisfying the same conditional centering constraints as H_j and H_{jk} in Appendix A.2. Hence f_L admits a discrete ANOVA-style decomposition mirroring the oracle decomposition of Proposition A.4.

In particular, the pairwise component

$$g_{jk}^L(Z_j, Z_k) := \phi_{jk}(Z)^\top \beta_{jk}^*$$

is the restriction of the orthogonal projection of f onto the subspace spanned by ϕ_{jk} , and can be interpreted as a binned approximation to the oracle residual surface $g_{jk}(X_j, X_k)$ on the $L \times L$ grid defined by (Z_j, Z_k) .

A.4. Finite-sample convergence of the surrogate interaction maps

We now show that the finite-sample ANOVA surrogate obtained by least squares on a sample $\{(X_i, Z_i)\}_{i=1}^n$ converges to the population projection described in Proposition A.7, and that the induced pairwise interaction maps converge accordingly.

Sampling model and empirical quantities. Let $\{X_i\}_{i=1}^n$ be an i.i.d. sample from P_X , and define $Z_i := q(X_i)$ for each i , where q is the fixed quantization map from Appendix A.1. We write

$$\phi_i := \phi(Z_i) \in \mathbb{R}^p, \quad f_i := f(X_i) \in \mathbb{R},$$

and define the empirical Gram matrix and cross-moment vector

$$\widehat{G}_n := \frac{1}{n} \sum_{i=1}^n \phi_i \phi_i^\top, \quad \widehat{b}_n := \frac{1}{n} \sum_{i=1}^n \phi_i f_i.$$

The finite-sample least-squares estimator is

$$\widehat{\beta}_n \in \arg \min_{\beta \in \mathbb{R}^p} \frac{1}{n} \sum_{i=1}^n (f_i - \beta^\top \phi_i)^2.$$

Whenever \widehat{G}_n is invertible, the solution is unique with the explicit form

$$\widehat{\beta}_n = \widehat{G}_n^{-1} \widehat{b}_n.$$

Assumption A.8 (i.i.d. sampling and moment conditions). The sample $(X_i)_{i \geq 1}$ is i.i.d. from P_X . Moreover, the basis $\phi(Z)$ is square-integrable in the sense that $\mathbb{E}[\|\phi(Z)\|_2^2] < \infty$ and $\mathbb{E}[\|\phi(Z)\|_2^2 f(X)^2] < \infty$.

Under Assumptions A.1, A.6, and A.8, the strong law of large numbers implies

$$\widehat{G}_n \xrightarrow{\text{a.s.}} G, \quad \widehat{b}_n \xrightarrow{\text{a.s.}} b,$$

where G and b are the population quantities in Proposition A.7.

Proposition A.9 (Finite-sample consistency of the ANOVA coefficients). *Under Assumptions A.1, A.2, A.6, and A.8, the empirical estimator $\widehat{\beta}_n$ exists and is unique with probability tending to one as $n \rightarrow \infty$, and*

$$\widehat{\beta}_n \xrightarrow{\text{a.s.}} \beta^*,$$

where β^* is the population projection coefficient vector from Proposition A.7.

Proof. By the strong law of large numbers and Assumption A.8, $\widehat{G}_n \rightarrow G$ and $\widehat{b}_n \rightarrow b$ almost surely. Since G is positive definite by Assumption A.6, all eigenvalues of G are strictly positive. Continuity of eigenvalues implies that \widehat{G}_n is positive definite (and hence invertible) for all sufficiently large n with probability one, so the empirical least-squares solution is unique and given by $\widehat{\beta}_n = \widehat{G}_n^{-1} \widehat{b}_n$ eventually almost surely.

The map $(G, b) \mapsto G^{-1}b$ is continuous on the set of positive definite matrices. Thus

$$\widehat{\beta}_n = \widehat{G}_n^{-1} \widehat{b}_n \xrightarrow{\text{a.s.}} G^{-1}b = \beta^*,$$

establishing the claim. \square

Convergence of surrogate predictors and interaction maps. The finite-sample ANOVA surrogate corresponding to $\widehat{\beta}_n$ is

$$\widehat{f}_{L,n}(Z) := \widehat{\beta}_n^\top \phi(Z),$$

and by grouping coefficients we can write

$$\widehat{f}_{L,n}(Z) = \widehat{\beta}_{0,n} + \sum_{j=1}^d \phi_j(Z)^\top \widehat{\beta}_{j,n} + \sum_{1 \leq j < k \leq d} \phi_{jk}(Z)^\top \widehat{\beta}_{jk,n},$$

where

$$\widehat{\beta}_n = (\widehat{\beta}_{0,n}, \{\widehat{\beta}_{j,n}\}_{j=1}^d, \{\widehat{\beta}_{jk,n}\}_{1 \leq j < k \leq d})$$

are the corresponding blocks.

For each pair (j, k) , the finite-sample interaction map on the discrete grid is

$$\widehat{g}_{jk,n}^L(z_j, z_k) := \phi_{jk}(z_j, z_k)^\top \widehat{\beta}_{jk,n}, \quad (z_j, z_k) \in \mathcal{G}_{jk},$$

whereas the population interaction map from Proposition A.7 is

$$g_{jk}^L(z_j, z_k) := \phi_{jk}(z_j, z_k)^\top \beta_{jk}^*.$$

Corollary A.10 (Finite-sample convergence of interaction maps). *Under the assumptions of Proposition A.9, for each pair (j, k) and each grid point $(z_j, z_k) \in \mathcal{G}_{jk}$,*

$$\widehat{g}_{jk,n}^L(z_j, z_k) \xrightarrow{\text{a.s.}} g_{jk}^L(z_j, z_k) \quad \text{as } n \rightarrow \infty.$$

Consequently,

$$\|\widehat{g}_{jk,n}^L - g_{jk}^L\|_{L^2(P_{Z_j, Z_k})} \xrightarrow{\text{a.s.}} 0.$$

Proof. For any fixed (j, k) and (z_j, z_k) ,

$$\widehat{g}_{jk,n}^L(z_j, z_k) - g_{jk}^L(z_j, z_k) = \phi_{jk}(z_j, z_k)^\top (\widehat{\beta}_{jk,n} - \beta_{jk}^*).$$

Since $\widehat{\beta}_{jk,n} \rightarrow \beta_{jk}^*$ almost surely by Proposition A.9, the right-hand side converges to zero almost surely for each fixed grid point. The grid \mathcal{G}_{jk} is finite, so we also have

$$\max_{(z_j, z_k) \in \mathcal{G}_{jk}} |\widehat{g}_{jk,n}^L(z_j, z_k) - g_{jk}^L(z_j, z_k)| \xrightarrow{\text{a.s.}} 0.$$

On a finite support, the $L^2(P_{Z_j, Z_k})$ -norm is bounded above by a constant multiple of the maximum absolute difference, hence

$$\|\widehat{g}_{jk,n}^L - g_{jk}^L\|_{L^2(P_{Z_j, Z_k})} \xrightarrow{\text{a.s.}} 0,$$

as claimed. \square

Remark A.11 (Uniform convergence over feature pairs). Since the number of feature pairs (j, k) is finite, the almost-sure convergence in Corollary A.10 can be strengthened to uniform convergence over all pairs:

$$\max_{1 \leq j < k \leq d} \|\widehat{g}_{jk,n}^L - g_{jk}^L\|_{L^2(P_{Z_j, Z_k})} \xrightarrow{\text{a.s.}} 0.$$

This uniform convergence will be used in the analysis of interaction strength consistency and Top- K /NDCG@ K alignment in Appendix A.5.

A.5. Interaction strength consistency and Top- K / NDCG@ K alignment

We now formalize how the finite-sample ANOVA surrogate yields interaction strengths that are consistent with their population counterparts and, under a margin condition, recover the oracle Top- K interaction pairs, implying alignment of NDCG@ K .

Interaction strength functionals. Recall the oracle residual surfaces $g_{jk}(x_j, x_k)$ and oracle strengths S_{jk}^* from Appendix A.1. Given a fixed quantization level L and the corresponding discrete maps g_{jk}^L from Appendix A.3, we define the discrete interaction strengths

$$S_{jk}^L := \|g_{jk}^L\|_{L^2(P_{Z_j, Z_k})} = \left(\mathbb{E}[g_{jk}^L(Z_j, Z_k)^2] \right)^{1/2}, \quad 1 \leq j < k \leq d.$$

At finite sample size n , the empirical discrete interaction strengths are

$$\widehat{S}_{jk,n}^L := \|\widehat{g}_{jk,n}^L\|_{L^2(P_{Z_j, Z_k})},$$

where $\widehat{g}_{jk,n}^L$ is the finite-sample interaction map defined in Appendix A.4.

Proposition A.12 (Consistency of discrete interaction strengths). *Under the assumptions of Corollary A.10, for each pair (j, k) ,*

$$\widehat{S}_{jk,n}^L \xrightarrow{a.s.} S_{jk}^L \quad \text{as } n \rightarrow \infty.$$

Moreover,

$$\max_{1 \leq j < k \leq d} |\widehat{S}_{jk,n}^L - S_{jk}^L| \xrightarrow{a.s.} 0.$$

Proof. For any fixed pair (j, k) ,

$$|\widehat{S}_{jk,n}^L - S_{jk}^L| = \left| \|\widehat{g}_{jk,n}^L\|_{L^2(P_{Z_j, Z_k})} - \|g_{jk}^L\|_{L^2(P_{Z_j, Z_k})} \right| \leq \|\widehat{g}_{jk,n}^L - g_{jk}^L\|_{L^2(P_{Z_j, Z_k})},$$

where the inequality follows from the reverse triangle inequality. Corollary A.10 implies that the right-hand side converges almost surely to zero, so $\widehat{S}_{jk,n}^L \rightarrow S_{jk}^L$ almost surely.

The uniform statement over all pairs follows by combining the reverse triangle inequality with the uniform convergence of interaction maps in Remark A.11:

$$\max_{j < k} |\widehat{S}_{jk,n}^L - S_{jk}^L| \leq \max_{j < k} \|\widehat{g}_{jk,n}^L - g_{jk}^L\|_{L^2(P_{Z_j, Z_k})} \xrightarrow{a.s.} 0.$$

□

Approximation of oracle strengths by discrete surrogates. To relate the discrete strengths S_{jk}^L back to the oracle strengths S_{jk}^* , we impose a mild regularity condition on g_{jk} and the grid refinement.

Assumption A.13 (Grid refinement and oracle strength approximation). There exists a sequence of quantization levels $L \rightarrow \infty$ such that for every pair (j, k) ,

$$\|g_{jk}^L - g_{jk}\|_{L^2(P_{X_j, X_k})} \xrightarrow{L \rightarrow \infty} 0.$$

Equivalently, the induced discrete strengths satisfy

$$\max_{1 \leq j < k \leq d} |S_{jk}^L - S_{jk}^*| \xrightarrow{L \rightarrow \infty} 0.$$

The equivalence between the L^2 -approximation of the interaction surfaces and the convergence of strengths follows from continuity of the L^2 -norm.

Top- K recovery under a margin condition. We now show that, if the oracle strengths exhibit a positive separation between the Top- K pairs and the remaining pairs, then the empirical discrete strengths recover the oracle Top- K set for sufficiently fine grids and sufficiently large samples.

For a fixed $K \in \{1, \dots, \binom{d}{2}\}$, let

$$\mathcal{T}_K^* \subseteq \{(j, k) : 1 \leq j < k \leq d\}$$

denote the set of indices corresponding to the Top- K oracle strengths, with ties broken arbitrarily but deterministically.

Assumption A.14 (Margin condition for Top- K strengths). There exists $\Delta > 0$ such that

$$\min_{(j,k) \in \mathcal{T}_K^*} S_{jk}^* - \max_{(j,k) \notin \mathcal{T}_K^*} S_{jk}^* \geq \Delta.$$

Theorem A.15 (Top- K interaction recovery). *Suppose Assumptions A.1, A.2, A.6, A.8, A.13, and A.14 hold. Then there exist $L_0 \in \mathbb{N}$ and $n_0 \in \mathbb{N}$ such that for all $L \geq L_0$ and all $n \geq n_0$,*

$$\widehat{\mathcal{T}}_{K,n}^L = \mathcal{T}_K^* \quad \text{almost surely,}$$

where $\widehat{\mathcal{T}}_{K,n}^L$ denotes the set of indices of the Top- K empirical strengths $\widehat{S}_{jk,n}^L$.

Proof. By Assumption A.13,

$$\max_{j < k} |S_{jk}^L - S_{jk}^*| \xrightarrow{L \rightarrow \infty} 0,$$

so there exists L_0 such that for all $L \geq L_0$,

$$\max_{j < k} |S_{jk}^L - S_{jk}^*| \leq \frac{\Delta}{4}.$$

By Proposition A.12, for any fixed L we have

$$\max_{j < k} |\widehat{S}_{jk,n}^L - S_{jk}^L| \xrightarrow[n \rightarrow \infty]{\text{a.s.}} 0,$$

so for each $L \geq L_0$ there exists a (random) finite $n_0(L)$ such that for all $n \geq n_0(L)$,

$$\max_{j < k} |\widehat{S}_{jk,n}^L - S_{jk}^L| \leq \frac{\Delta}{4} \quad \text{almost surely.}$$

Combining the two bounds yields, for all $L \geq L_0$ and $n \geq n_0(L)$,

$$\max_{j < k} |\widehat{S}_{jk,n}^L - S_{jk}^*| \leq \max_{j < k} |\widehat{S}_{jk,n}^L - S_{jk}^L| + \max_{j < k} |S_{jk}^L - S_{jk}^*| \leq \frac{\Delta}{2} \quad \text{almost surely.}$$

Now fix such L and n , and consider any $(j, k) \in \mathcal{T}_K^*$ and $(m, n) \notin \mathcal{T}_K^*$. By the margin condition (Assumption A.14),

$$S_{jk}^* \geq S_{mn}^* + \Delta.$$

Using the uniform error bound,

$$\widehat{S}_{jk,n}^L \geq S_{jk}^* - \frac{\Delta}{2} \geq S_{mn}^* + \frac{\Delta}{2} \geq \widehat{S}_{mn,n}^L,$$

almost surely. Thus every Top- K oracle pair has strictly larger empirical strength than every non-Top- K pair, so the Top- K sets coincide: $\widehat{\mathcal{T}}_{K,n}^L = \mathcal{T}_K^*$ almost surely. Taking $n_0 := \max_{L_0 \leq L \leq L_1} n_0(L)$ for any fixed finite L_1 and then letting $L_1 \rightarrow \infty$ yields the stated result. \square

NDCG@K alignment. We finally connect Top- K recovery to the ranking metric NDCG@K. Let G_{jk}^* denote the oracle “gain” associated with pair (j, k) , for example $G_{jk}^* = S_{jk}^*$ or a monotone transform thereof. Given a permutation π of the pairs, the (unnormalized) DCG@K of π with respect to G^* is

$$\text{DCG@K}(\pi; G^*) := \sum_{\ell=1}^K \frac{G_{\pi(\ell)}^*}{\log_2(\ell+1)},$$

and the ideal DCG@K is obtained by using the permutation π^* that ranks pairs in decreasing order of G^* :

$$\text{IDCG@K}(G^*) := \text{DCG@K}(\pi^*; G^*).$$

The corresponding NDCG@K is

$$\text{NDCG@K}(\pi; G^*) := \frac{\text{DCG@K}(\pi; G^*)}{\text{IDCG@K}(G^*)}.$$

In our setting, π_n is the permutation induced by the empirical strengths $\widehat{S}_{jk,n}^L$, and π^* is the oracle permutation induced by S_{jk}^* .

Corollary A.16 (NDCG@K alignment). *Under the assumptions of Theorem A.15, we have*

$$\text{NDCG@K}(\pi_n; G^*) \xrightarrow[n \rightarrow \infty]{a.s.} 1,$$

for any choice of gains $G_{jk}^* = g(S_{jk}^*)$ where $g : \mathbb{R}_+ \rightarrow \mathbb{R}_+$ is strictly increasing.

Proof. By Theorem A.15, for sufficiently large L and n the Top- K set induced by $\widehat{S}_{jk,n}^L$ coincides with the oracle Top- K set \mathcal{T}_K^* , and the ordering within this set matches the ordering induced by S_{jk}^* (since the margin condition yields strict inequalities). Because g is strictly increasing, the gains $G_{jk}^* = g(S_{jk}^*)$ preserve this ordering.

Thus, for all sufficiently large L and n , the permutation π_n coincides with the oracle permutation π^* on the first K positions almost surely, which implies

$$\text{DCG@K}(\pi_n; G^*) = \text{DCG@K}(\pi^*; G^*) = \text{IDCG@K}(G^*)$$

and hence $\text{NDCG@K}(\pi_n; G^*) = 1$. Therefore $\text{NDCG@K}(\pi_n; G^*) \rightarrow 1$ almost surely. \square

A.6. Equivalence to classical 2^5 factorial designs

We now make precise the sense in which, on the synthetic 2^5 factorial benchmark used in the experiments, the discrete ANOVA surrogate becomes algebraically equivalent to a classical two-level factorial design analysis.

Synthetic 2^5 factorial setup. Consider five binary factors

$$U_j \in \{-1, +1\}, \quad j = 1, \dots, 5,$$

and let $U = (U_1, \dots, U_5)$ be uniformly distributed over the full 2^5 factorial design, so that each configuration $u \in \{-1, +1\}^5$ has probability 2^{-5} . The synthetic response is

$$f^*(u) = \beta_0 + \sum_{j=1}^5 \beta_j u_j + \sum_{1 \leq j < k \leq 5} \gamma_{jk} u_j u_k,$$

with fixed coefficients $\beta_0 \in \mathbb{R}$, $\beta_j \in \mathbb{R}$, and $\gamma_{jk} \in \mathbb{R}$. In the experiments, the trained predictor f is fitted to noisy observations of f^* , but for the purposes of this appendix we work at the population level and identify f with f^* .

To match the discrete ANOVA framework, we define a two-level quantization map

$$q_j(u_j) := \begin{cases} 1, & u_j = -1, \\ 2, & u_j = +1, \end{cases} \quad j = 1, \dots, 5,$$

and set $Z_j = q_j(U_j) \in \{1, 2\}$, $Z = (Z_1, \dots, Z_5)$.

Classical 2^5 factorial contrasts. In the standard two-level factorial analysis, one introduces contrast codings

$$x_j := U_j \in \{-1, +1\}, \quad x_{jk} := U_j U_k \in \{-1, +1\},$$

and forms the design matrix

$$X = [\mathbf{1}, x_1, \dots, x_5, x_{12}, x_{13}, \dots, x_{45}] \in \mathbb{R}^{32 \times p},$$

where $\mathbf{1}$ is the all-ones column and $p = 1 + 5 + 10 = 16$ is the number of intercept, main-effect, and pairwise-interaction contrasts. The least-squares coefficients of the linear model f^* coincide with $(\beta_0, \{\beta_j\}, \{\gamma_{jk}\})$ up to the usual scaling conventions.

ANOVA basis on $\{1, 2\}^5$. On the discrete variables $Z_j \in \{1, 2\}$, we take an ANOVA basis

$$\phi(Z) = (\phi_0(Z), \{\phi_j(Z)\}_{j=1}^5, \{\phi_{jk}(Z)\}_{1 \leq j < k \leq 5}) \in \mathbb{R}^p,$$

with the following structure:

- $\phi_0(Z) \equiv 1$,
- $\phi_j(Z)$ is a one-dimensional contrast for Z_j , centered under the uniform distribution on $\{1, 2\}$,
- $\phi_{jk}(Z)$ is a collection of two-dimensional contrasts on (Z_j, Z_k) , centered under the uniform distribution on $\{1, 2\}^2$ and orthogonal to ϕ_j and ϕ_k .

A concrete choice consistent with Appendix A.3 is

$$\phi_j(Z) = c_j (\mathbf{1}\{Z_j = 2\} - \mathbf{1}\{Z_j = 1\}) \propto U_j,$$

and similarly one can choose $\phi_{jk}(Z)$ such that one of its coordinates is proportional to $U_j U_k$ and the remaining coordinates span the orthogonal complement (these additional coordinates are irrelevant for f^* since it depends only on $U_j U_k$).

Evaluating ϕ on the 2^5 design points yields the ANOVA design matrix

$$\Phi = [\phi(Z^{(1)}), \dots, \phi(Z^{(32)})]^\top \in \mathbb{R}^{32 \times p},$$

where $\{Z^{(i)}\}_{i=1}^{32}$ enumerate all configurations in $\{1, 2\}^5$.

Proposition A.17 (Equivalence to classical 2^5 factorial design). *Consider the synthetic 2^5 factorial setting above, with $f = f^*$ and two-level quantization q . Then:*

1. *There exists an invertible matrix $T \in \mathbb{R}^{p \times p}$ such that the ANOVA design matrix Φ and the classical factorial design matrix X satisfy*

$$\Phi = XT.$$

2. *The population ANOVA surrogate $f_L(Z) = \beta^{*\top} \phi(Z)$ from Proposition A.7 coincides with $f^*(U)$ on the 2^5 design:*

$$f_L(Z) = f^*(U) \quad \text{almost surely.}$$

3. *The ANOVA coefficient blocks $(\beta_0^*, \{\beta_j^*\}, \{\beta_{jk}^*\})$ are an invertible linear reparameterization of $(\beta_0, \{\beta_j\}, \{\gamma_{jk}\})$. In particular, for each pair (j, k) ,*

$$g_{jk}^L(Z_j, Z_k) = \phi_{jk}(Z)^\top \beta_{jk}^* = c_{jk} \gamma_{jk} U_j U_k,$$

for some nonzero constant c_{jk} depending only on the chosen contrast scaling.

4. *The target ANOVA interaction strengths satisfy*

$$S_{jk}^* = \|g_{jk}\|_{L^2(P_{U_j, U_k})} \propto |\gamma_{jk}|,$$

and the discrete strengths S_{jk}^L from Appendix A.5 satisfy

$$S_{jk}^L = \|g_{jk}^L\|_{L^2(P_{Z_j, Z_k})} \propto |\gamma_{jk}|,$$

with the same ordering over pairs (j, k) .

Proof of 1. Each column of X is a $\{-1, +1\}$ -valued contrast on the uniform design, and the ANOVA columns in Φ are obtained from X by rescaling and (within blocks) mixing columns that span the same contrast subspaces for intercept, main effects, and two-factor interactions. Since both sets of columns form bases of the same p -dimensional subspace of \mathbb{R}^{32} (the space of all functions on the 2^5 grid that are at most pairwise in the U_j), there exists an invertible linear map T such that $\Phi = XT$. \square

Proof of 2. The synthetic f^* is exactly linear in the columns of X , so there exists a coefficient vector $\theta \in \mathbb{R}^p$ with

$$f^*(U) = X\theta$$

on the 2^5 design. Writing $\beta^* := T^{-1}\theta$ yields

$$\Phi\beta^* = XTT^{-1}\theta = X\theta = f^*(U),$$

so the ANOVA surrogate $f_L(Z) = \beta^{*\top}\phi(Z)$ interpolates f^* exactly on all design points. \square

Proof of 3. The equivalence $\Phi = XT$ and the exact interpolation in *Proof of 2.* imply that the ANOVA coefficients β^* are related to the classical factorial coefficients θ by the invertible linear map $\beta^* = T^{-1}\theta$. Decomposing θ into blocks $(\beta_0, \{\beta_j\}, \{\gamma_{jk}\})$ and β^* into blocks $(\beta_0^*, \{\beta_j^*\}, \{\beta_{jk}^*\})$ gives the desired reparameterization. Since f^* depends on (U_j, U_k) only through the product $U_j U_k$ with coefficient γ_{jk} , the corresponding pairwise ANOVA component g_{jk}^L must be proportional to $U_j U_k$, with proportionality constant $c_{jk} \neq 0$ determined by the chosen contrast normalization. \square

Proof of 4. For the oracle surface,

$$g_{jk}(u_j, u_k) = \gamma_{jk} u_j u_k,$$

and under the uniform distribution on $\{-1, +1\}^2$,

$$S_{jk}^* = \|g_{jk}\|_{L^2(P_{U_j, U_k})} = \left(\mathbb{E}[\gamma_{jk}^2 U_j^2 U_k^2]\right)^{1/2} = |\gamma_{jk}|.$$

For the discrete ANOVA component in *Proof of 3.*,

$$S_{jk}^L = \|g_{jk}^L\|_{L^2(P_{Z_j, Z_k})} = |c_{jk}| |\gamma_{jk}| \|U_j U_k\|_{L^2(P_{U_j, U_k})} = C_{jk} |\gamma_{jk}|,$$

for some constant $C_{jk} > 0$ depending only on the contrast scaling. In either case, the mapping $(j, k) \mapsto S_{jk}^*$ and $(j, k) \mapsto S_{jk}^L$ are strictly monotone in $|\gamma_{jk}|$, so they induce the same ordering over feature pairs. \square

Remark A.18 (Interpretation for the synthetic benchmark). Proposition A.17 shows that, on the synthetic 2^5 factorial benchmark, the ANOVA surrogate coincides with the classical factorial analysis: the surrogate is an exact representation of the ground truth f^* , and the interaction strengths are monotone in the true interaction coefficients γ_{jk} . This explains why, in the experiments, the oracle-based metrics (NDCG@K, Peak-IoU, and Xfer-NDCG@K) can be interpreted as probing how well an explanation method recovers the standard factorial interaction structure on its natural home ground.

A.7. Further theoretical remarks: grid resolution, misspecification, and higher-order terms

We collect here several complementary remarks that clarify how the ANOVA surrogate behaves as the grid resolution varies, how to interpret the construction under model misspecification, and what is implicitly assumed about higher-order interactions.

Remark A.19 (Grid resolution and joint approximation error). Combining the discretization error in Assumption A.13 with the finite-sample results in Appendix A.4 yields a simple decomposition of the total approximation error between the empirical surrogate interactions and the target ANOVA interaction strengths.

For each pair (j, k) and quantization level L , extend the discrete surface g_{jk}^L to a function of (X_j, X_k) by composing with the quantization map, i.e.

$$\tilde{g}_{jk}^L(X_j, X_k) := g_{jk}^L(q_j(X_j), q_k(X_k)),$$

and similarly

$$\widehat{g}_{jk,n}^L(X_j, X_k) := \widehat{g}_{jk,n}^L(q_j(X_j), q_k(X_k)).$$

Then for each (j, k) ,

$$\|\widehat{g}_{jk,n}^L - g_{jk}\|_{L^2(P_{X_j, X_k})} \leq \|\widehat{g}_{jk,n}^L - \widetilde{g}_{jk}^L\|_{L^2(P_{X_j, X_k})} + \|\widetilde{g}_{jk}^L - g_{jk}\|_{L^2(P_{X_j, X_k})}.$$

The first term on the right-hand side is controlled by the finite-sample convergence of the discrete maps in Corollary A.10, while the second term is the pure discretization error in Assumption A.13. In particular, for any sequence of grid levels $L_n \rightarrow \infty$ such that

$$\max_{j < k} \|\widetilde{g}_{jk}^{L_n} - g_{jk}\|_{L^2(P_{X_j, X_k})} \xrightarrow{n \rightarrow \infty} 0,$$

and any sampling regime in which

$$\max_{j < k} \|\widehat{g}_{jk,n}^{L_n} - \widetilde{g}_{jk}^{L_n}\|_{L^2(P_{X_j, X_k})} \xrightarrow[n \rightarrow \infty]{\text{a.s.}} 0,$$

we also obtain

$$\max_{j < k} \|\widehat{g}_{jk,n}^{L_n} - g_{jk}\|_{L^2(P_{X_j, X_k})} \xrightarrow[n \rightarrow \infty]{\text{a.s.}} 0.$$

Heuristically, this formalizes the bias–variance tradeoff in L : finer grids reduce the discretization bias but require more samples to stably estimate the corresponding coefficients.

Remark A.20 (Misspecification and dependence on P_X). All oracle quantities in Appendix A.2 are defined as orthogonal projections in the Hilbert space $L^2(P_X)$ of the trained predictor f . In particular, the main-effect and interaction components (m_j, g_{jk}) and the residual r are defined by their $L^2(P_X)$ -best approximation properties, regardless of whether f arises from a “correctly specified” probabilistic model.

Two important consequences are:

- The interaction surfaces g_{jk} and strengths S_{jk}^* reflect both the architecture and the data distribution P_X . If the same predictor f were evaluated under a different input distribution, the oracle decomposition and strengths would, in principle, change.
- When the true mechanism contains higher-order or non-factorizable structure, these contributions are distributed across the pairwise surfaces g_{jk} and the residual r in the way that minimizes $L^2(P_X)$ error. Our oracle is therefore “model-centric”: it asks how f can be best approximated by main and pairwise terms under the observed P_X , rather than asserting that g_{jk} coincides with a causal or structural notion of two-way interaction.

In the presence of misspecification, our evaluation metrics should thus be interpreted as comparing explanation methods against this canonical projection-based oracle, not against a latent ground-truth mechanism that may or may not align with $L^2(P_X)$ geometry.

Remark A.21 (Higher-order interactions and extensions). The analysis in Appendices A.2–A.5 explicitly truncates the ANOVA decomposition at order two, i.e. it uses

$$\mathcal{H}_{\leq 2} = H_0 \oplus \left(\bigoplus_j H_j \right) \oplus \left(\bigoplus_{j < k} H_{jk} \right)$$

as the target subspace. Higher-order terms are absorbed into the residual $R = \mathcal{H}_{\leq 2}^\perp$. Formally, one could extend the construction to include third- and higher-order subspaces

$$H_{jkl}, H_{jklm}, \dots$$

defined by the usual ANOVA centering constraints, and construct an oracle interaction hierarchy up to any fixed order q . The main reasons we restrict attention to pairwise terms in this work are:

- *Statistical and computational cost.* The number of q -way interactions grows as $\binom{d}{q}$, and the corresponding grids scale as L^q . Even for moderate d , maintaining stable estimates beyond $q = 2$ quickly becomes prohibitive under realistic sample sizes.
- *Interpretability.* Empirically, pairwise interaction surfaces already provide a rich and visual summary of non-additive structure. Higher-order visualizations become difficult to inspect and compare across methods.

From the perspective of our evaluation framework, the truncation to pairwise terms means that all methods, including the oracle itself, are judged on their ability to recover the best pairwise approximation to f in $L^2(P_X)$. In settings where specific higher-order interactions are of primary interest, one could in principle repeat the analysis with $\mathcal{H}_{\leq q}$ for $q > 2$, at the cost of substantially increased computational and sample requirements.

B. Additional implementation details

After fitting the factorial surrogate in the ANOVA basis, we apply a lightweight post-processing step to enforce discrete ANOVA-style constraints on the main-effect and interaction tables. This step consists of (i) centering each main-effect table to have zero mean over its levels, (ii) centering each pairwise interaction table so that all row and column sums vanish, and (iii) absorbing any constant offsets induced by these operations into the global mean $\hat{\mu}$. The procedure is summarized in Algorithm 1; it requires only a few passes over the discrete tables and is negligible compared to training the backbone or fitting the surrogate.

Algorithm 1 Residual centering and μ -rebalancing of ANOVA tables

Require: Global mean $\hat{\mu}$, main-effect tables $\{\hat{m}_j\}_{j=1}^d$, interaction tables $\{\hat{g}_{jk}\}_{1 \leq j < k \leq d}$

```

1: // Center main effects
2: for  $j = 1$  to  $d$  do
3:    $\bar{m}_j \leftarrow \frac{1}{|\mathcal{B}_j|} \sum_{\ell_j \in \mathcal{B}_j} \hat{m}_j(\ell_j)$ 
4:   for each  $\ell_j \in \mathcal{B}_j$  do
5:      $\hat{m}_j(\ell_j) \leftarrow \hat{m}_j(\ell_j) - \bar{m}_j$ 
6:   end for
7: end for
8: // Center interactions and accumulate mean shift
9:  $\Delta\mu \leftarrow 0$ 
10: for each pair  $(j, k)$  with  $j < k$  do
11:    $\bar{g}_{jk} \leftarrow \frac{1}{|\mathcal{B}_j||\mathcal{B}_k|} \sum_{\ell_j, \ell_k} \hat{g}_{jk}(\ell_j, \ell_k)$ 
12:    $\Delta\mu \leftarrow \Delta\mu + \bar{g}_{jk}$ 
13:   for all  $(\ell_j, \ell_k)$ :  $\hat{g}_{jk}(\ell_j, \ell_k) \leftarrow \hat{g}_{jk}(\ell_j, \ell_k) - \bar{g}_{jk}$ 
14:   subtract row means so that  $\sum_{\ell_j} \hat{g}_{jk}(\ell_j, \ell_k) = 0$  for all  $\ell_k$ 
15:   subtract column means so that  $\sum_{\ell_k} \hat{g}_{jk}(\ell_j, \ell_k) = 0$  for all  $\ell_j$ 
16: end for
17:  $\hat{\mu} \leftarrow \hat{\mu} + \Delta\mu$ 

```

Ensure: Centered tables $\hat{\mu}$, $\{\hat{m}_j\}$, $\{\hat{g}_{jk}\}$ satisfying discrete ANOVA-style constraints

C. Additional Experimental Results

In this section we report the full numerical results for all five metrics on the three main regression benchmarks. For each dataset, we provide one table with point estimates and one table with the corresponding 95% confidence intervals.

On the Synthetic 2^5 factorial benchmark, the point estimates in Table 3 show that ORACLE achieves perfect interaction selection ($\text{NDCG}@5 = 1.0000$) and near-perfect cross-backbone transfer ($\text{Xfer-NDCG}@5 \approx 1.00$), while all SHAP-family baselines also perform strongly but fall slightly behind in $\text{NDCG}@5$. In terms of scale alignment, the concordance coefficient CCC is substantially larger for ORACLE than for the baselines, indicating a closer match between surrogate and oracle interaction strengths. Peak-IoU@0.10 is essentially zero for ORACLE because, by construction, the target ANOVA interaction maps on this synthetic task are extremely concentrated on a few design points, leaving little room for localized hotspot overlap at the chosen resolution. All methods achieve the same best-case intervention gain $\text{IG}@5,3$. The confidence intervals in Table 4 confirm that these patterns are stable across seeds: the intervals for $\text{NDCG}@5$ and $\text{Xfer-NDCG}@5$ are tightly concentrated near one for ORACLE, and CCC maintains a clear gap over the SHAP-family methods.

On Airfoil, the point estimates in Table 5 illustrate a more realistic low-dimensional physical regression setting. ORACLE again attains the highest $\text{NDCG}@5$ and $\text{Xfer-NDCG}@5$ among all methods, together with the largest Peak-IoU@0.10, indicating that the ANOVA surrogate not only recovers the most important interaction pairs but also localizes the main non-additive hotspots more accurately on the 2D grids. The SHAP-family baselines exhibit lower $\text{NDCG}@5$ and Xfer -

Table 3. Interaction metrics on Synthetic (point estimates).

Metric	ORACLE	FSI	SHAP-IQ	SVARM-IQ	KS-Int	DS-Int
NDCG@5	1.0000	0.8868	0.9981	0.9472	0.9996	0.8688
CCC	0.6427	0.0348	0.0448	0.0418	0.0655	0.0342
Peak-IoU@0.10	0.0000	0.0333	0.1333	0.1117	0.1500	0.1400
Xfer-NDCG@5	0.9979	0.9381	0.9338	0.9672	0.9989	0.9289
IG@K=5,B=3	1.5962	1.5962	1.5962	1.5962	1.5962	1.5962

Table 4. Interaction metrics on Synthetic (95% confidence intervals).

Metric	ORACLE	FSI	SHAP-IQ	SVARM-IQ	KS-Int	DS-Int
NDCG@5	[1.0000, 1.0000]	[0.8124, 1.0000]	[0.9883, 1.0000]	[0.9228, 1.0000]	[0.9935, 1.0000]	[0.7593, 1.0000]
CCC	[0.5061, 0.7038]	[0.0181, 0.0700]	[0.0259, 0.0663]	[0.0210, 0.0852]	[0.0369, 0.0894]	[0.0171, 0.0636]
Peak-IoU@0.10	[0.0000, 0.0000]	[0.0000, 0.1000]	[0.0333, 0.3000]	[0.0333, 0.1884]	[0.0500, 0.2333]	[0.0333, 0.2467]
Xfer-NDCG@5	[0.9837, 1.0000]	[0.8985, 1.0000]	[0.8737, 1.0000]	[0.8799, 1.0000]	[0.9886, 1.0000]	[0.8619, 1.0000]
IG@K=5,B=3	[0.4043, 1.5962]	[0.4043, 1.5962]	[0.4043, 1.5962]	[0.4043, 1.5962]	[0.4043, 1.5962]	[0.4043, 1.5962]

NDCG@5 and noticeably smaller Peak-IoU@0.10, but some of them achieve competitive IG@5,3, reflecting that a subset of their top-ranked interactions still yields strong intervention-oriented gains. The CCC values are uniformly small on this dataset, underscoring that matching the target ANOVA interaction strengths scale is challenging even when the ranking and spatial patterns are reasonably accurate. Table 6 shows that these observations are robust: the confidence intervals for ORACLE in NDCG@5, Peak-IoU@0.10, and Xfer-NDCG@5 remain consistently above those of the baselines, while most CCC intervals for the SHAP-family methods include zero.

Table 5. Interaction metrics on Airfoil (point estimates).

Metric	ORACLE	FSI	SHAP-IQ	SVARM-IQ	KS-Int	DS-Int
NDCG@5	0.9085	0.7320	0.7638	0.6705	0.7994	0.7462
CCC	0.1411	0.0385	0.0105	0.0236	0.0346	0.0147
Peak-IoU@0.10	0.2000	0.1000	0.1000	0.1667	0.1333	0.1667
Xfer-NDCG@5	0.9555	0.7702	0.7736	0.6989	0.7938	0.7585
IG@K=5,B=3	2.7597	2.2812	2.7597	2.7153	2.7597	2.7597

On kin8nm, a moderately large nonlinear regression problem, the point estimates in Table 7 highlight a mixed but still favorable picture for ORACLE. It achieves the highest NDCG@5 and Xfer-NDCG@5, and the largest Peak-IoU@0.10, suggesting strong performance in both interaction selection and hotspot localization, as well as stable transfer across backbones. Among the SHAP-family baselines, KS-Int is the strongest competitor, with high NDCG@5 and Xfer-NDCG@5 and the second-best CCC, while other variants trade off selection performance for slightly improved scale alignment. The IG@5,3 scores show that several baselines can sometimes match or approach the best intervention gains, even when their rankings and maps are less faithful in aggregate. The confidence intervals in Table 8 indicate that these trends are statistically significant: the intervals for ORACLE in NDCG@5, Peak-IoU@0.10, and Xfer-NDCG@5 are consistently shifted upward relative to the SHAP-family methods, whereas CCC shows overlapping but systematically higher intervals for ORACLE and KS-Int compared to the other baselines.

Overall, across all three benchmarks and all five metrics, the additional results in Tables 3–8 support the main-paper findings: ANOVA-based surrogates (ORACLE) provide strong and stable advantages in interaction selection, hotspot localization, and cross-backbone transfer, while SHAP-family interactions can offer partially complementary strengths, particularly in some aspects of scale alignment and intervention-oriented utility.

D. Classical Main-Effect and Interaction Plots

ANOVA. Table 9 reports an ANOVA-style variance decomposition of the ORACLE surrogate trained on Airfoil (Backbone A). Among the main effects, *Frequency* and *Suction side* dominate the contribution to model variation: their sums

Table 6. Interaction metrics on Airfoil (95% confidence intervals).

Metric	ORACLE	FSI	SHAP-IQ	SVARM-IQ	KS-Int	DS-Int
NDCG@5	[0.6866, 1.0000]	[0.5799, 1.0000]	[0.5504, 1.0000]	[0.5225, 0.9863]	[0.5914, 0.9989]	[0.4787, 0.9816]
CCC	[0.0379, 0.1965]	[-0.0214, 0.0936]	[-0.0398, 0.0839]	[-0.0302, 0.0833]	[-0.0224, 0.0834]	[-0.0379, 0.1070]
Peak-IoU@0.10	[0.1000, 0.3000]	[0.0000, 0.2000]	[0.0000, 0.2000]	[0.0000, 0.4000]	[0.0333, 0.2333]	[0.0000, 0.4000]
Xfer-NDCG@5	[0.7613, 1.0000]	[0.5916, 1.0000]	[0.5801, 1.0000]	[0.4897, 0.9901]	[0.5880, 1.0000]	[0.5187, 0.9946]
IG@K=5,B=3	[1.0478, 2.7597]	[1.2913, 2.7597]	[1.2913, 2.7597]	[1.1944, 2.7597]	[1.1944, 2.7597]	[1.1944, 2.7597]

Table 7. Interaction metrics on kin8nm (point estimates).

Metric	ORACLE	FSI	SHAP-IQ	SVARM-IQ	KS-Int	DS-Int
NDCG@5	0.9921	0.6130	0.8122	0.8309	0.9446	0.8077
CCC	0.3730	0.1333	0.2088	0.1470	0.3182	0.1701
Peak-IoU@0.10	0.3571	0.0833	0.0714	0.0595	0.1190	0.0833
Xfer-NDCG@5	0.9931	0.6031	0.8278	0.8106	0.9182	0.7269
IG@K=5,B=3	1.5214	1.1501	1.4829	1.5214	1.4829	1.4829

of squares are roughly 1.4×10^4 and 8.5×10^3 , respectively, clearly larger than those of *Chord length*, *Angle of attack*, and *Free stream*. In the normalized %Total column, these two factors alone account for about 18.2% and 11.1% of the overall ORACLE importance, while the remaining main effects are comparatively modest. On the interaction side, the pairs *Frequency:Chord length*, *Frequency:Suction side*, *Angle of attack:Suction side*, and *Angle of attack:Chord length* exhibit particularly large sums of squares and %Total values in the mid single digits, revealing strong non-additive structure between these factors. Interactions involving *Free stream* (e.g., *Frequency:Free stream*, *Chord length:Free stream*) are present but comparatively weaker. The residual term still carries about 26.3% of the normalized total contribution, which indicates that a pure two-way ORACLE decomposition does not capture all higher-order or fine-grained nonlinear effects, and that the table is best viewed as a screening device for the most influential factors and pairs.

From a practical perspective, we recommend using the ANOVA-style table in Table 9 as a first-stage diagnostic before examining the classical plots shown later in this section.

1. Ranking rows by *Sum Sq* or the normalized %Total quickly identifies the main effects and interactions that account for most of the ORACLE importance (here, *Frequency*, *Suction side*, and their interactions).
2. The %Expl. column rescales contributions relative to the explained variance only (i.e., excluding the residual term), and is therefore useful for understanding how the most important terms share the portion of variation that the two-way ORACLE surrogate is actually able to capture.
3. The residual %Total provides a simple diagnostic of how faithfully the two-way decomposition approximates the full ORACLE surrogate: when the residual contribution is small, patterns in the main-effect and interaction plots can be read as describing most of the predictor’s behaviour; when the residual is large, it is safer to focus interpretation on the top few main and interaction terms and to treat the remaining structure as higher-order or model-specific detail.

The main-effect plots and classical interaction plots that follow make these decomposition findings visually explicit by showing how the predicted sound-pressure level changes along each factor and how the most important pairs reinforce or counteract each other across their joint ranges.

Main effects. Figure 2 shows classical main-effect plots of the ORACLE surrogate on Airfoil (Backbone A). Each panel displays the marginal response

$$x_j \mapsto \mu + m_j(x_j)$$

evaluated on the bin centers used by ORACLE. Several patterns are immediately visible. First, *Frequency* and *Suction side* exhibit the largest vertical ranges, matching their dominant sums of squares in Table 9: increasing the frequency from low to high values steadily reduces the predicted sound-pressure level, while larger suction-side displacement thickness is associated with a pronounced decrease in SPL after a sharp peak at very small values. Second, *Chord length* also shows

Table 8. Interaction metrics on kin8nm (95% confidence intervals).

Metric	ORACLE	FSI	SHAP-IQ	SVARM-IQ	KS-Int	DS-Int
NDCG@5	[0.9288, 1.0000]	[0.4677, 0.8682]	[0.5958, 0.9574]	[0.6642, 0.9991]	[0.6986, 1.0000]	[0.5823, 0.9642]
CCC	[0.2788, 0.4297]	[0.0818, 0.2591]	[0.1520, 0.2768]	[0.0961, 0.1980]	[0.1663, 0.4618]	[0.1213, 0.2397]
Peak-IoU@0.10	[0.1786, 0.5357]	[0.0238, 0.1667]	[0.0238, 0.1253]	[0.0238, 0.1071]	[0.0476, 0.2143]	[0.0357, 0.1310]
Xfer-NDCG@5	[0.9340, 1.0000]	[0.4447, 0.8733]	[0.6105, 0.9795]	[0.5811, 0.9994]	[0.7019, 0.9940]	[0.5091, 0.9301]
IG@K=5,B=3	[1.0438, 1.5214]	[0.9512, 1.4829]	[0.9522, 1.4829]	[0.9522, 1.5214]	[0.8517, 1.4829]	[1.0438, 1.5214]

Table 9. ANOVA-style decomposition of the ORACLE surrogate on Airfoil (Backbone A).

Source	Sum Sq	%Total	%Expl.	Rank	Cum%Tot
Frequency	14049.600	18.2	53.4	1	18.2
Angle of attack	2540.306	3.3	9.7	9	21.5
Chord length	3998.431	5.2	15.2	5	26.7
Free stream	1550.353	2.0	5.9	12	28.7
Suction side	8535.002	11.1	32.4	2	39.8
Frequency:Angle of attack	1557.488	2.0	5.9	11	41.8
Frequency:Chord length	5410.700	7.0	20.6	3	48.8
Frequency:Free stream	599.716	0.8	2.3	15	49.6
Frequency:Suction side	4667.970	6.1	17.7	4	55.6
Angle of attack:Chord length	3645.811	4.7	13.9	7	60.4
Angle of attack:Free stream	1398.027	1.8	5.3	13	62.2
Angle of attack:Suction side	3984.059	5.2	15.1	6	67.3
Chord length:Free stream	654.140	0.8	2.5	14	68.2
Chord length:Suction side	2563.853	3.3	9.7	8	71.5
Free stream:Suction side	1691.144	2.2	6.4	10	73.7
Residual	20295.598	26.3			100.0
Total	46611.280	100.0			

a mostly monotone decreasing trend, whereas *Free stream* shows a mild increasing trend over its range. Finally, *Angle of attack* displays a weakly curved, non-monotone pattern with a broad maximum around moderate angles, suggesting a smaller but nontrivial main effect.

From a usage perspective, we find the following simple heuristics helpful when reading Figure 2:

1. Compare the *vertical range* in each panel; larger ranges indicate factors with stronger main effects and should roughly agree with the ordering in the ANOVA table. This provides a quick visual sanity check that the surrogate decomposition is consistent.
2. Inspect the *shape* of each curve: near-linear trends suggest approximately additive, monotone effects that are easy to reason about and to intervene on (e.g., “lower frequency \Rightarrow lower SPL”), whereas pronounced curvature or non-monotonicity (as for *Angle of attack* and *Suction side*) reveals regimes where the effect changes sign or saturates.
3. Use the bin centers on the *x-axis* as candidate design points for one-factor-at-a-time interventions: by moving along the curve in Figure 2, practitioners can anticipate how much reduction in SPL is attainable by adjusting a single factor while keeping the others near their empirical distribution.

These main-effect plots thus complement the ANOVA-style table: the table ranks factors by overall contribution, while Figure 2 makes the direction, strength, and nonlinearity of each effect visually explicit.

Interaction plots. While Figure 2 visualises how each factor acts on its own, Figure 3 shows how pairs of factors jointly shape the ORACLE surrogate on Airfoil. Each panel in the upper-triangular grid corresponds to a pair (X_j, X_k) , with the horizontal axis indexing bins of the column factor X_k and the three lines representing low, medium, and high bins (Bin 0,

Bin 2, Bin 4) of the row factor X_j . Non-additive structure appears as *non-parallel* or *crossing* lines: when the lines remain roughly parallel, changing the row factor shifts the response up or down by an almost constant offset, whereas clearly diverging slopes indicate that the effect of X_k depends strongly on the level of X_j .

Consistent with the ANOVA table in Table 9, several panels in Figure 3 display pronounced interactions. For example, the *Frequency:Chord length* and *Frequency:Suction side* panels show that the SPL response to *Chord length* or *Suction side* can either increase or decrease depending on whether frequency is in a low or high bin, with the three lines clearly spreading out and sometimes reversing order across the x -axis. In contrast, weaker interaction pairs such as those involving *Free stream* often exhibit nearly parallel lines: the response level changes with the row factor, but the qualitative shape along the column factor is preserved, which is closer to an additive effect.

In practice, we suggest reading Figure 3 using the following heuristics:

1. Start from the pairs with large interaction sums of squares in Table 9 and verify that their panels show clearly non-parallel or crossing lines. This cross-check ensures that the numerical interaction ranking aligns with visually interpretable patterns.
2. Within a given panel, treat the three lines (Bin 0, 2, 4) as a coarse “design grid”: steep changes in slope or reversals between lines mark regimes where simultaneous adjustment of both factors can yield larger gains than tuning either factor alone.
3. For panels with almost parallel lines, interpret the corresponding pair as approximately additive and fall back to the main-effect plots in Figure 2 when reasoning about interventions. This helps focus attention on a small number of genuinely interacting pairs rather than over-interpreting small visual deviations.

Together, Figure 2 and Figure 3 provide a DoE-style summary of the ORACLE surrogate: the former highlights which single factors matter most and in which direction, while the latter localises where in the input space pairs of factors reinforce or counteract each other.

E. Latent Extensions with ResNet and BERT

This section extends our evaluation to latent tabular features extracted from image and text models, and illustrates the methodological regime where grid-based ANOVA surrogates become less favorable than perturbation-based SHAP interactions.

ResNet-18 on CIFAR-10. Tables 10 and 11 summarize interaction metrics on latent tabular features extracted by ResNet-18 from CIFAR-10. On this image-derived representation, SHAP-family interaction methods consistently achieve higher NDCG@5 and Xfer-NDCG@5 than ORACLE, and also obtain larger CCC and IG@K=5,B=3, indicating better alignment with the target ANOVA interaction strengths and greater best-case intervention gains relative to the ANOVA-based target. The confidence intervals in Table 11 show that these gaps are substantial and robust, with several SHAP variants reaching the upper bound of IG@K=5,B=3 induced by the target interaction maps. In contrast, ORACLE remains comparatively competitive in hotspot overlap (Peak-IoU@0.10), suggesting that its spatial localization of interaction hotspots is less degraded than its ranking and scale estimates in this image-latent regime.

Table 10. Interaction metrics on ResNet-18 features from CIFAR-10. Rows report mean scores over feature pairs for detection (NDCG@5), hotspot overlap (Peak-IoU@0.10), cross-backbone transfer (Xfer-NDCG@5), scale alignment (CCC), and intervention gain (IG@K=5,B=3). Columns correspond to interaction explanation methods.

Metric	ORACLE	FSI	SHAP-IQ	SVARM-IQ	KS-Int	DS-Int
NDCG@5	0.7192	0.8988	0.8821	0.8866	0.8237	0.9262
CCC	0.0386	0.0687	0.0464	0.0703	0.1235	0.0484
Peak-IoU@0.10	0.1786	0.1071	0.0595	0.1190	0.1071	0.0714
Xfer-NDCG@5	0.7167	0.8808	0.8759	0.8396	0.8475	0.8674
IG@K=5,B=3	1.8529	3.3345	3.3345	3.0305	2.2825	3.0757

Table 11. 95% bootstrap confidence intervals for the ResNet-18 / CIFAR-10 interaction metrics in Table 10. Each entry reports the lower and upper bounds of the interval.

Metric	ORACLE	FSI	SHAP-IQ	SVARM-IQ	KS-Int	DS-Int
NDCG@5	[0.5630, 0.8780]	[0.8367, 0.9843]	[0.7377, 0.9659]	[0.7700, 0.9919]	[0.7107, 0.9832]	[0.7784, 1.0000]
CCC	[0.0020, 0.0923]	[0.0294, 0.1139]	[0.0211, 0.0811]	[0.0367, 0.1100]	[0.0765, 0.1667]	[0.0204, 0.0798]
Peak-IoU@0.10	[0.0357, 0.3571]	[0.0476, 0.1938]	[0.0238, 0.1104]	[0.0595, 0.2024]	[0.0476, 0.1699]	[0.0238, 0.1494]
Xfer-NDCG@5	[0.6009, 0.8493]	[0.7987, 0.9852]	[0.7029, 0.9718]	[0.7254, 0.9627]	[0.7908, 0.9509]	[0.7435, 0.9564]
IG@K=5,B=3	[1.0900, 3.2424]	[1.7940, 3.3345]	[1.7045, 3.3345]	[1.8032, 3.3345]	[1.8594, 3.2957]	[1.0303, 3.0769]

BERT-base on AG News. Tables 12 and 13 report interaction metrics on latent tabular features extracted from BERT-base embeddings of AG News. Similar to the ResNet-18 / CIFAR-10 case, SHAP-family interaction methods generally attain higher NDCG@5 and Xfer-NDCG@5 than ORACLE, and several baselines (in particular KS-Int) achieve markedly larger CCC values, indicating better alignment with the scale of the target ANOVA interaction strengths. ORACLE again remains most competitive in hotspot localization: it attains the highest Peak-IoU@0.10 among all methods, suggesting that its spatial interaction maps still track the hotspots of the target ANOVA maps relatively well even when its ranking and scale estimates are weaker. The confidence intervals in Table 13 show that these patterns are robust, with most SHAP variants overlapping near-perfect detection while ORACLE maintains consistently strong Peak-IoU@0.10.

Table 12. Interaction metrics on BERT-base features from AG News. Rows report mean scores over feature pairs for detection (NDCG@5), hotspot overlap (Peak-IoU@0.10), cross-backbone transfer (Xfer-NDCG@5), scale alignment (CCC), and intervention gain (IG@K=5,B=3). Columns correspond to interaction explanation methods.

Metric	ORACLE	FSI	SHAP-IQ	SVARM-IQ	KS-Int	DS-Int
NDCG@5	0.8117	0.9262	0.8554	0.8935	0.9648	0.9177
CCC	0.0596	0.0964	0.0855	0.1181	0.1943	0.1134
Peak-IoU@0.10	0.1667	0.0833	0.1190	0.1429	0.0952	0.1310
Xfer-NDCG@5	0.7525	0.8201	0.8064	0.8425	0.7648	0.8101
IG@K=5,B=3	1.9288	1.8326	1.6207	1.9288	1.9224	1.6207

Table 13. 95% bootstrap confidence intervals for the BERT-base / AG News interaction metrics in Table 12. Each entry reports the lower and upper bounds of the interval.

Metric	ORACLE	FSI	SHAP-IQ	SVARM-IQ	KS-Int	DS-Int
NDCG@5	[0.6153, 1.0000]	[0.6625, 1.0000]	[0.6164, 1.0000]	[0.7268, 0.9924]	[0.8023, 1.0000]	[0.7854, 1.0000]
CCC	[0.0123, 0.0962]	[0.0334, 0.1448]	[0.0326, 0.1271]	[0.0616, 0.1559]	[0.0794, 0.2875]	[0.0451, 0.1719]
Peak-IoU@0.10	[0.0952, 0.2500]	[0.0357, 0.1310]	[0.0562, 0.2089]	[0.0714, 0.2262]	[0.0238, 0.1667]	[0.0682, 0.2143]
Xfer-NDCG@5	[0.5045, 0.9631]	[0.5735, 0.9809]	[0.5576, 0.9534]	[0.6076, 0.9856]	[0.4776, 0.9756]	[0.6343, 0.9836]
IG@K=5,B=3	[1.1298, 1.9288]	[1.1826, 1.9515]	[1.2198, 1.9762]	[1.3080, 1.9399]	[1.3303, 2.0453]	[1.0999, 2.0399]

Analysis of latent-domain performance. Across Tables 10–13, SHAP-family interaction methods generally outperform ORACLE on NDCG@5, Xfer-NDCG@5, CCC, and IG@K=5,B=3, while ORACLE remains comparatively competitive only in Peak-IoU@0.10. This pattern is consistent with the design bias of our approach: ORACLE is tailored to low- to medium-dimensional factor-style or tabular inputs, where binning along each coordinate and fitting an orthogonal ANOVA surrogate yields an accurate piecewise-constant approximation of the predictor. In contrast, the 8D PCA latents of ResNet-18 and BERT encode highly entangled, nonlocal, and often higher-order semantic interactions; under such representations, the L -bin ANOVA projection becomes more biased, and small perturbations within a bin can have effects that are poorly captured by a constant cell value. SHAP-family methods instead probe the predictor via interventional feature subsets without relying on a particular binning scheme, and thus transfer more robustly to these continuous embeddings. Overall, these results reinforce that ORACLE’s strengths are most pronounced on structured tabular factors with interpretable coordinates, whereas Shapley-style interactions provide more reliable rankings and scales on image and text latent features, with ORACLE retaining some advantage primarily in spatial hotspot overlap.

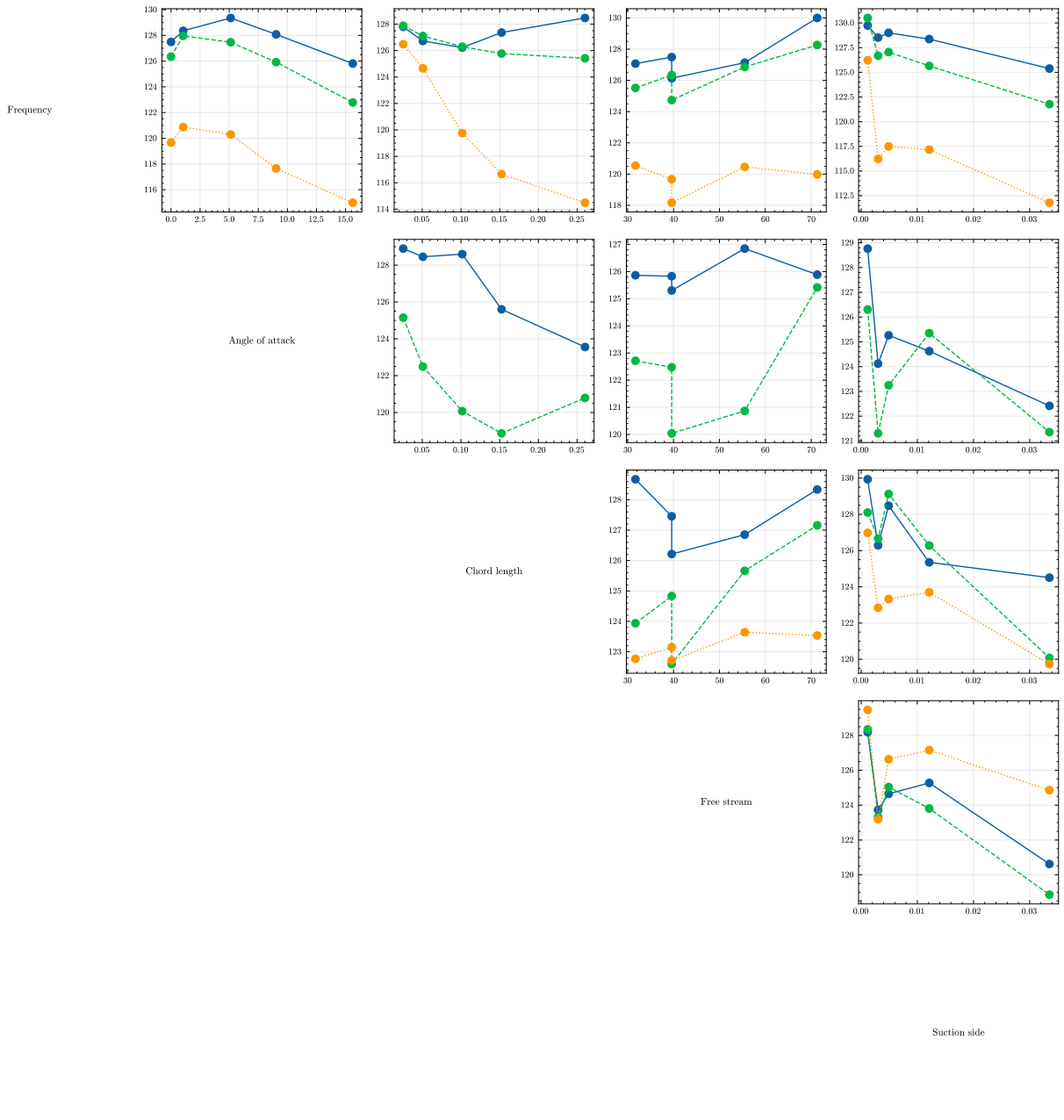


Figure 3. Classical ORACLE interaction plots for the Airfoil dataset (Backbone A). Rows and columns correspond to factors; each upper-triangular panel shows the predicted SPL across bins of the column factor for three representative bins (Bin 0, Bin 2, Bin 4) of the row factor. Non-parallel or crossing lines indicate strong non-additive interactions, while nearly parallel lines correspond to approximately additive behaviour.